united nations
educational, scientific
and cultural
organization

international atomic
energy agency

the
abdus salam
international centre for theoretical physics

SMR/1328/19

School on the Physics of Equatorial Atmosphere

(24 September - 5 October 2001)

Synthesis: Equatorial Ionospheric Morphology at Large and Small Scales

M. A. Abdu
(Instituto Nacional de Pesquisas Espaciais, São José dos Campos, Brazil)

Synthesis: Equatorial ionospheric morphology at large and small scales

(Abdu)

The ionosphere -thermosphere -atmosphere coupling, involving the wind system, dynamo electric field, and plasma fountain are the major factors that determine the equatorial ionosphere phenomena and their morphology at large and small scales. A schematic representation of the coupling processes that form the basis of the phenomenology is shown in **Fig.1.**

The dynamo electric field generated by the tidal wind system at E layer heights (a) establishes the quiet time ionospheric current system, and (b) being mapped on to the equatorial F layer heights produces the plasma fountain that controls the plasma density distribution of the tropical ionosphere. The electric field produced by the F layer dynamo becomes dominant only after sunset when the E layer electron density, and therefore the conductivity, decays due to recombination. While the electric fields, driven by the wind system are the immediate driving forces for the major phenomena during day and night, the wind system that produce these electric field, act in a more direct way also to control the morphology of these phenomena.

The major equatorial phenomena are: 1- the electrojet current systems and associated plasma structures, 2- ionization anomaly and associated anomalies in the neutral temperature and wind; 3- spread –F /plasma bubbles structures of the nighttime ionosphere.

The local time dependence of the major phenomena that result from the coupling processes is shown in **Fig.2.**

The equatorial electric fields and their temporal variations serve as the immediate cause of the spatial and temporal variations in the phenomenology, and the morphology of the equatorial ionosphere-thermosphere system. The equatorial electric field pattern for different season as obtained from Jicamarca radar observations is shown in **Fig 3**. An empirical model of the electric field for different longitude sectors of the globe, based on the AE-E satellite data and Jicamarca radar observations, are presented in **Fig. 4.**

Morphology at large scale:

Daytime electric field, which is eastward, produces, under the E×B force, upward plasma drift constituting the daytime plasma fountain. An example of the low latitude plasma drift pattern resulting from the combined action of an upward E X B drift near the equator and a downward diffusion along the magnetic field lines resulting from a numerical model calculation is shown in **Fig.5.**

This fountain is responsible for the formation of the ionization peaks in the subtropics on both sides of anomaly. An example of a simulation using a numerical computer code showing the low latitude ionization crests symmetrically formed on either side of an equatorial trough is shown in **Fig. 6.**

An example of latitudinal distribution of NmF2 /TEC as a function of local time modeled for different values of equatorial electric field is shown in **Fig. 7**. Larger electric field produces more intense and broader ionization anomaly. Observational evidence showing the control of equatorial electric field on the formation of the equatorial anomaly is presented in **Fig 8.**

Plasma drift pattern as a result of combined actions including the effect of a trans-equatorial meridional wind resulting from simulation by the Sheffield University Plasmasphere-ionosphere model (SUPIM) is shown in **Fig. 9** for conditions representative of three longitude sectors, Fortaleza Brazil), Jicamarca (Peru) and Thumba (India). A trans-equatorial wind can cause asymmetric formation of the anomaly peaks, with the height of the F2 layer being lower (higher) on the down wind (upwind) hemisphere, as the example of a model calculation presented in **Fig. 10**.

The ionospheric morphology determined by these electrodynamic processes can go through large variations with longitude, due to the longitudinal variation in the geomagnetic field configuration over the low latitude region as shown in the global maps of the magnetic field intensity and declination angle of **Fig.11**.

Especially, the magnetic anomaly characterized by a global minimum of intensity, in the South Atlantic and Brazil, and the associated large magnetic declination angle, produce important deviation in the ionospheric morphology of this longitude sector as compared to other longitude sectors, some aspects of which also will considered here.

An example of the equatorial anomaly pattern in electron density as observed from ground based and satellite born topside sounders are shown in Figs.**12 a, b. and c**. Some additional morphological features of NmF2, hmF2 and TEC over low latitude are shown in **Figures 13.**

A recent phenomenon of the equatorial F layer being investigated concerns the formation of an additional layer above the F2 peak, known as the F3 layer. The F3 layer has been observed at locations close to the dip equator during daytime more frequently around pre noon hours. The layer was first observed over Fortaleza in Brazil. The mechanism of its formation has been investigated with the help of the Sheffield University Plasmasphere-Ionosphere Model (SUPIM) by Balan et al. (199?). Its occurrence pattern on a long-term basis has been studied by Batista et al. (2001). Some results are presented in Figs. **14, 15 and 16.**

Equatorial anomaly has been observed also in thermospheric zonal wind and temperature by Dynamic explorer satellite that is associated with the ionization anomaly. An example is shown in **Fig.17**.

Morphology at small scale.

Equatorial spread F

As compared to the temporal and spatial scales of the morphological features described above, the equatorial spread F structures have morphological features at much smaller scales, although the plasma bubble structures that envelop spread F irregularities have scale sizes of 100s of kilometers perpendicular to field line and thousands of kilometer extension along the field line.

The equatorial F layer height increases in the evening hours under the action of an enhanced zonal (eastward) electric field, known as prereversal enhancement electric field. This feature representing low and high solar activity conditions is shown in **Fig.18**. Such layer uplift is a prerequisite for the occurrence of spread F irregularities that may last for several following hours of the night.

The local time distribution of Spread F, as observed in ionograms, is presented in **Fig.19**. It is plotted in the form of its monthly mean percentage occurrence representing low and high solar activity years. These results are for the equatorial station Fortaleza and the anomaly crest (low latitude) location Cachoeira Paulista in Brazil. The post sunset ESF onset, rapid increase in the occurrence rate during the first 1-2 hours attaining peak activity around ~22 LT and the gradual decay towards morning hours, and the seasonal variation in these patterns are evident in this figure.

Latitudinal distribution of spread F occurrence as obtained from topside sounder data shows that the irregularity belt is confined to ±20° in latitude as presented in **Fig.20**. A representation of the global statistical distribution of scintillation occurrence is presented in **Fig 21**, which shows the pattern of local time-latitude extension of the scintillation producing structures.

The seasonal variation of spread F irregularity occurrence is longitude dependent. Over Brazil the season of maximum occurrence is centered around December solstice as was evident in **Fig.19**. However, over Jicamarca/Huancayo, Peru which is ~30°west of the Brazilian stations the spread F occurrence presents mostly equinoctial maximums. Such features are shown for the cases of ionogram spread F and UHF scintillation in **Figs. 22 and 23** respectively.

Such differences in the seasonal pattern of spread F occurrence are associated with the difference magnetic declination angle that characterize these longitude sectors as was pointed out with reference to **Fig.11**. It is known that a first order requirement for the initiation of spread F is the large prereversal enhancement electric field that causes the uplift of the F layer in the post sunset hours. The amplitude of the prereversal enhancement attains a maximum when the solar terminator becomes aligned with magnetic meridian whereby near simultaneous sunset occurs at conjugate E layers, a condition that is fulfilled in December solstice over Brazil (due to the large westward declination angle, ~22°W in this sector), and during equinoctial months over Peru (where the declination angle is small, ~4°E). The seasonal variation of scintillation occurrence pattern for different longitude sectors of the globe is presented in **Fig. 24** which seems to confirm the magnetic declination control of the seasonal pattern in the irregularity, suggested from the comparison spread F data form Brazil and Peru.

The spread F occurrence depends positively on the solar UV radiation represented by the F10.7 flux. Such dependence arises because the prereversal electric field enhancement amplitude also increases with increase of solar flux as shown in **Fig.25**. A statistical dependence of spread F occurrence on F10.7 is presented in **Fig.26**. **(The figures 25 and 26 are not included here)**

Equatorial electrojet Irregularities:

Fig.1- A schematic of the ionosphere-thermosphere coupling processes.

Fig.2- Local time dependence of the major phenomena of the equatorial ionosphere.

Fig.3- Equatorial zonal electric field/vertical plasma drift as observed by the Jicamarca radar as mean values representing different seasons.

Fig.4- Empirical model of global electric variation pattern for different longitude sectors based on data from AE-E satellite.

Fig.5- Plasma drift pattern at low latitudes due to the combined action of an upward E X B drift near the magnetic equator and a downward diffusion along B (Hanson and Moffett, JGR. 71, 5559, 1066).

Fig.6- An example of electron density distribution of the equatorial ionization anomaly showing two crests in subtropics symmetrically on either sides of the equator, resulting from numerical model.

Fig.7- Latitudinal distribution of NmF2, the maximum density of the F2 layer as modeled by a numerical code for different values of the equatorial electric field, (a) zero electric field, (b) average electric field, (c) strong electric field.

Fig.8- HmF2 over Fz and foF2 over Cachoeira Paulista and ΔH over Fz, to demonstrate the control of electric field on the formation of the anomaly.

Fig.9- Plasma fountain resulting from the combined actions of E X B, diffusion along field lines and meridional (trans-equatorial) wind for three longitude sectors, Fortaleza (Brazil, Jicamarca (Peru), and Thumba (India), resulting from SUPIM (Balan et al., 199?).

Fig.10-Calculated electron density contours as a function of latitude and dip latitude at 2000 LT for December conditions (Anderson and Roble, JATP, 43, 835, 1981). 10b- An asymmetric equatorial anomaly for the Brazilian sector.

Fig.11-Magnitude of the geomagnetic field (top) and declination angle in degrees (bottom) at the Earth's surface.

Fig.12 a- Equatorial anomaly in electron density distribution mapped by ground based sounders, b- Anomaly as observed by a topside sounder, c-

Fig.13-Examples of morphological features of NmF2, hmF2, TEC etc. over low latitude. (a) foF2 and hmF2 over Fortaleza, (b)- foF2 and hmF2 over Cachoeira Paulista,

Fig.14-Some examples of F3 layer observed over Fortaleza.

Fig.15-SUPIM simulations of the F3 layer formation by the combined action of electric filed and meridional wind (Balan et al., 199?).

Fig.16-Long term F3 layer occurrence statistics over Fortaleza (Batista et al., 2001)

Fig.17-Equatorial Wind and Temperature anomaly showing latitudinal features that are associated with those of the ionization anomaly.

Fig.18-The F layer height (h'F) over Fortaleza showing the evening uplift of the layer under the evening enhanced eastward electric field.

Fig.19-Spead F occurrence over Fortaleza and Cachoeira Paulista (Brazil) in monthly mean percentage values plotted for all months for years representing low and high solar activity conditions.

Fig.20 a and b -Latitudinal distribution of spread F form ground based and satellite topside sounding observations.

Fig.21-Global pattern of scintillation distribution (AFGL Hand book, 1985).

Fig.22-Spread F monthly mean distribution for an year showing the seasonal pattern of its occurrence over Huancayo (Rastogi, JGR, 85, 722, 1980)

Fig.23-Statistical distribution of UHF scintillation occurrence over Peru (Basu et al., Geophys. Res. Letts., 7, 259, 1980)

Fig.24-Seasonal variation of scintillation occurrence at different longitude sectors of the globe showing that maximum in the occurrence could occur near the nodal point of the conjugate E layer sunset local times, which is controlled by the magnetic declination angle (Tsunoda, JGR, 1985).

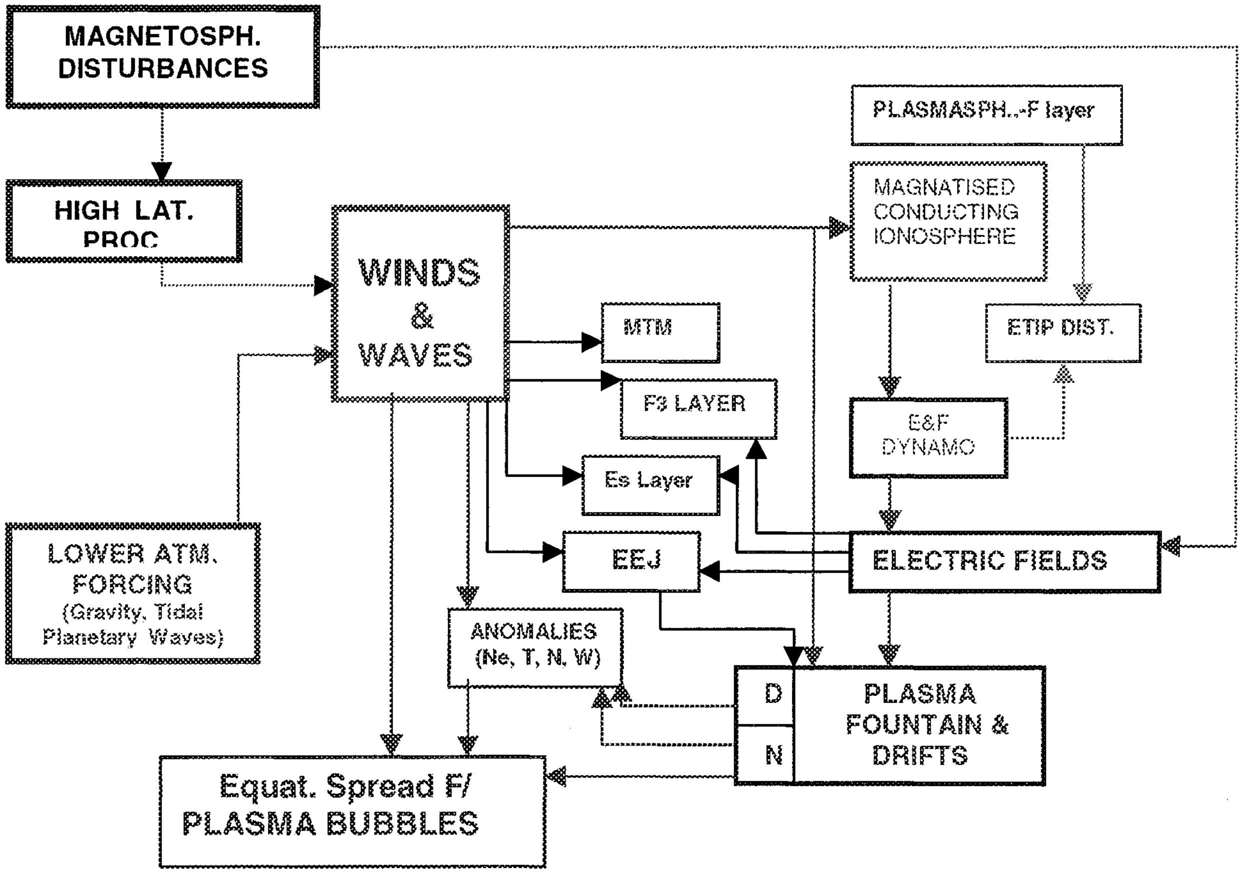

EQUATORIAL IONOSPHERE-ATMOSPHERE-THERMOSPHERE COUPLING PROCESSES

Fig. 1

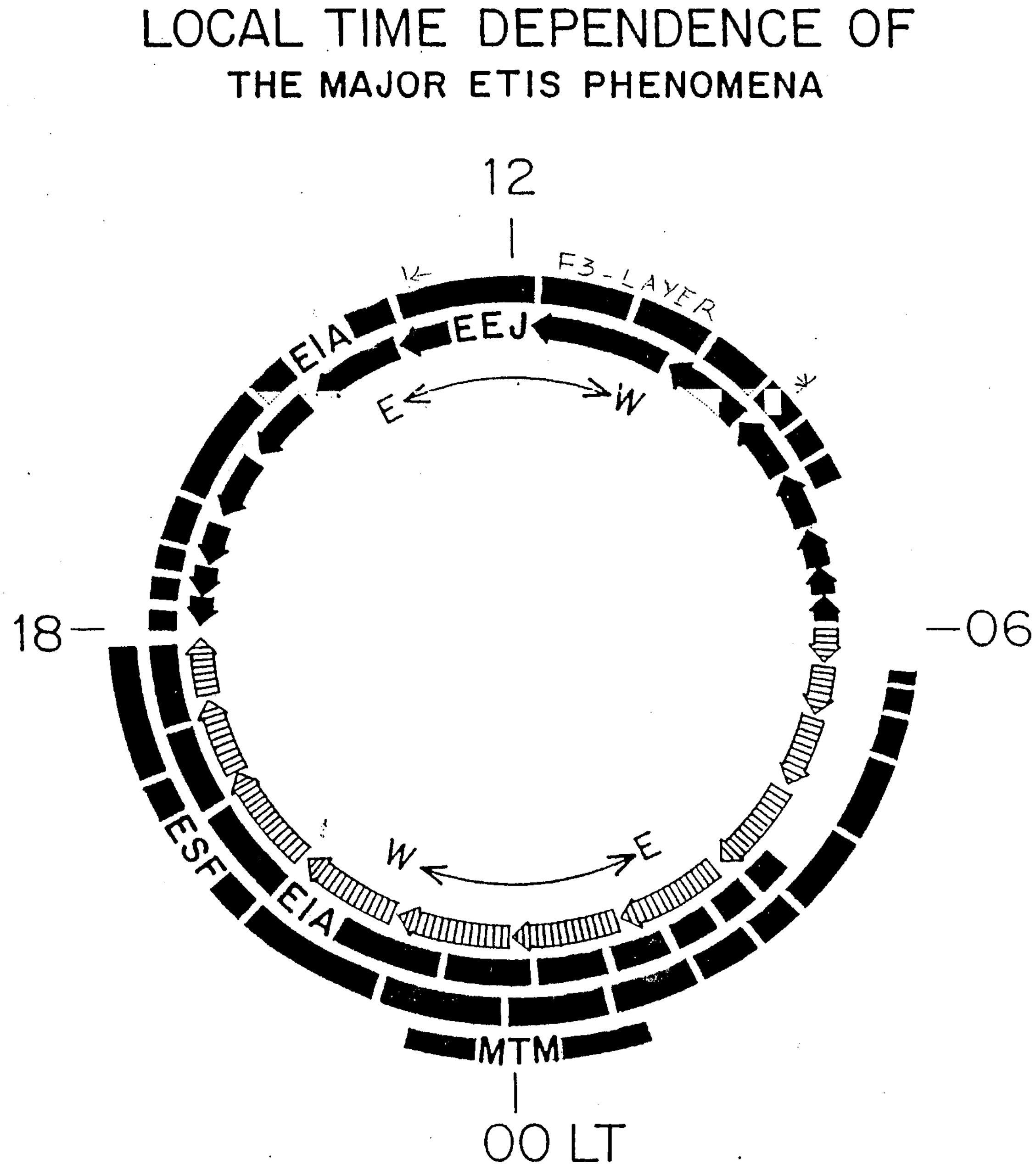
LOCAL TIME DEPENDENCE OF
THE MAJOR ETIS PHENOMENA
12
F3-LAYER
EEJ
EIA
E
W
18
06
ESF
EIA
W
E
MTM
00 LT

Fig. 02

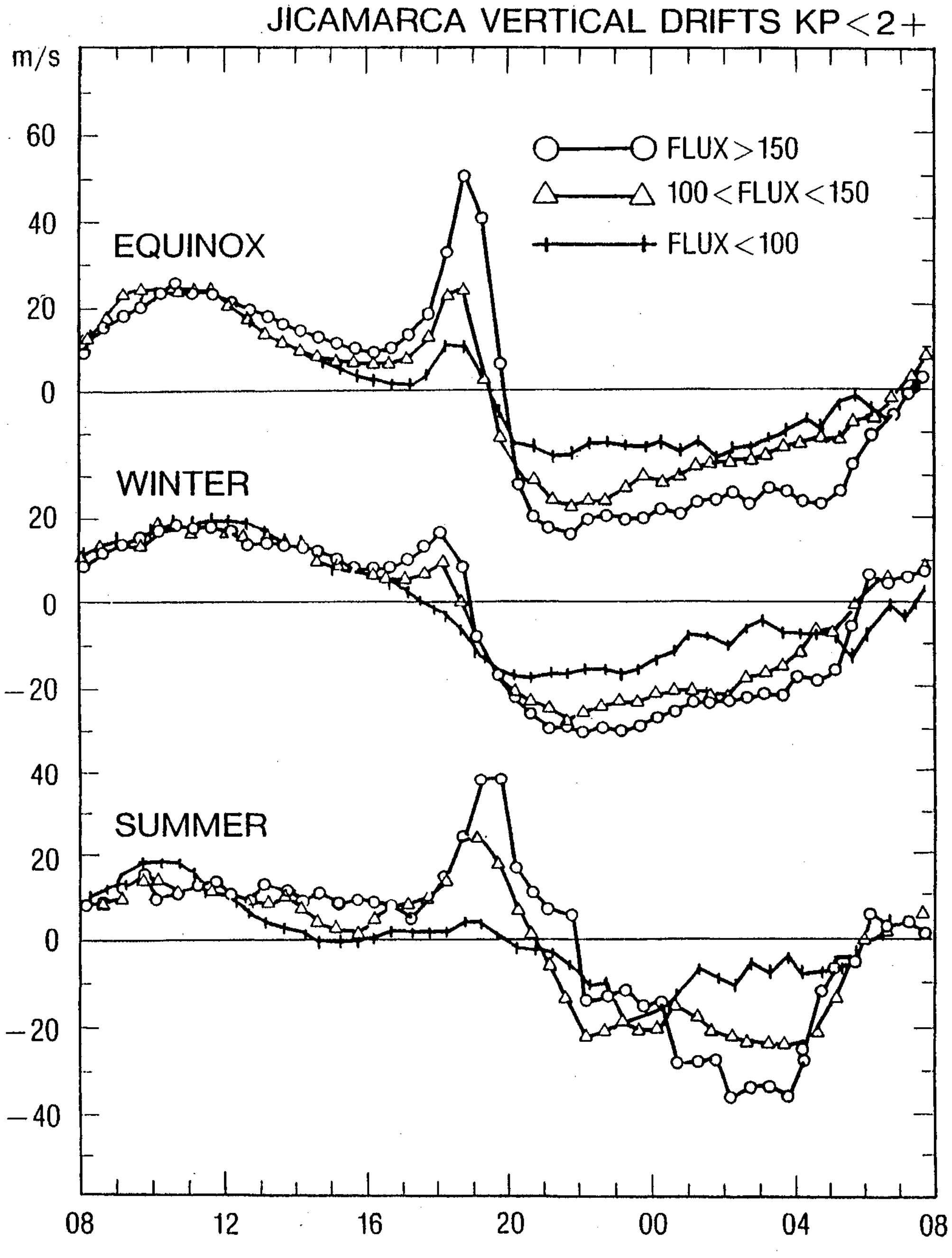
JICAMARCA VERTICAL DRIFTS KP<2+
m/s
60
40
20
0
20
0
−20
40
20
0
−20
−40
EQUINOX
WINTER
SUMMER
FLUX>150
100<FLUX<150
FLUX<100
08
12
16
20
00
04
08
LOCAL TIME (75°W)

Fig. 03

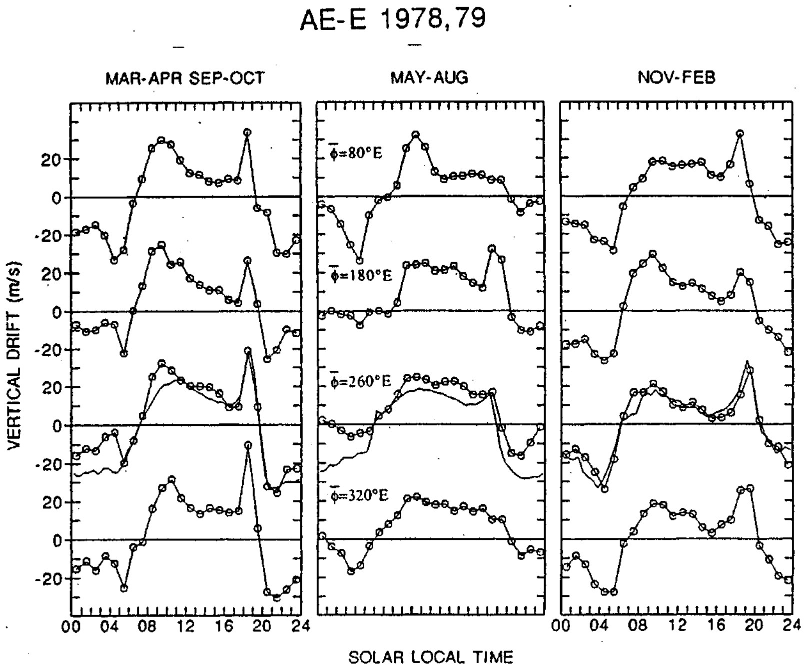

Empirical model of the satellite vertical drifts at four longitudinal sectors for moderate to high solar flux conditions and magnetically quiet conditions. Here $\bar{\phi}$ denotes the average east longitudes. The seasonal Jicamarca drifts patterns for similar solar flux and geomagnetic conditions are also shown.

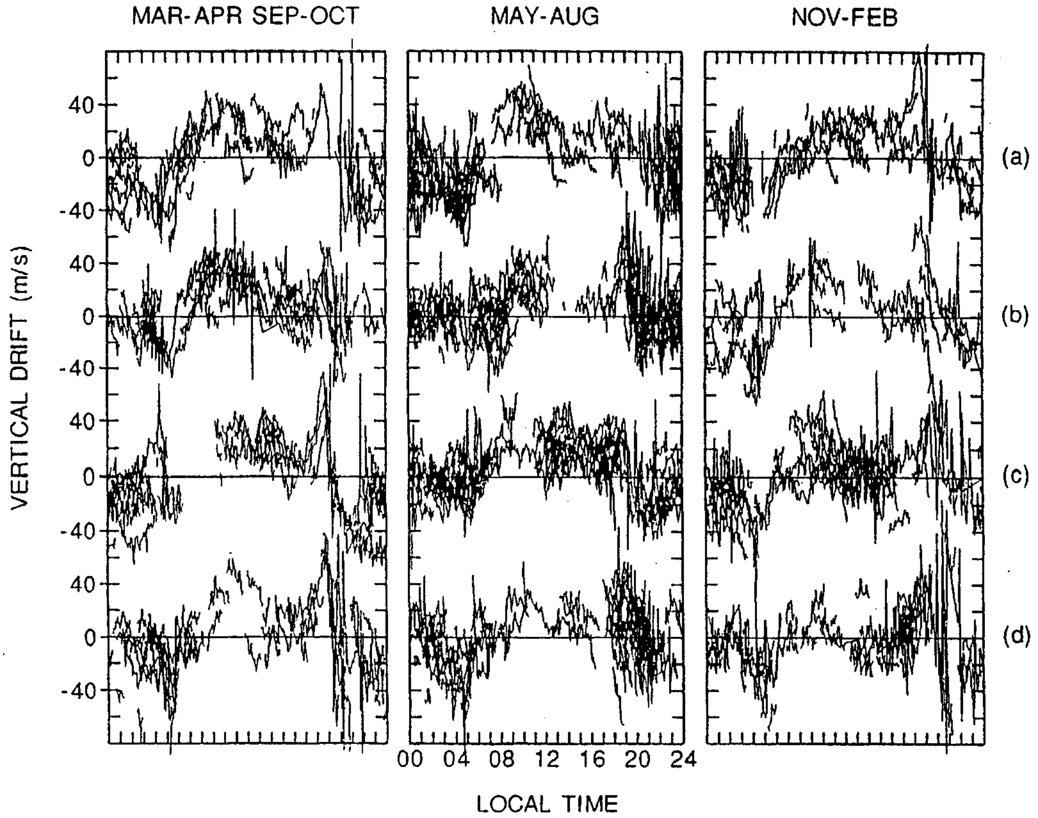

Scatter plot of the 1978-1979 AE-E vertical drifts at four longitudinal sectors representative of the (a) African-Indian (0°-150° E), (b) the Pacific (150°-210° E), (c) the Western American (210°-300° E), and (d) the Brazilian (300°-360° E) equatorial regions.

Fig. 04

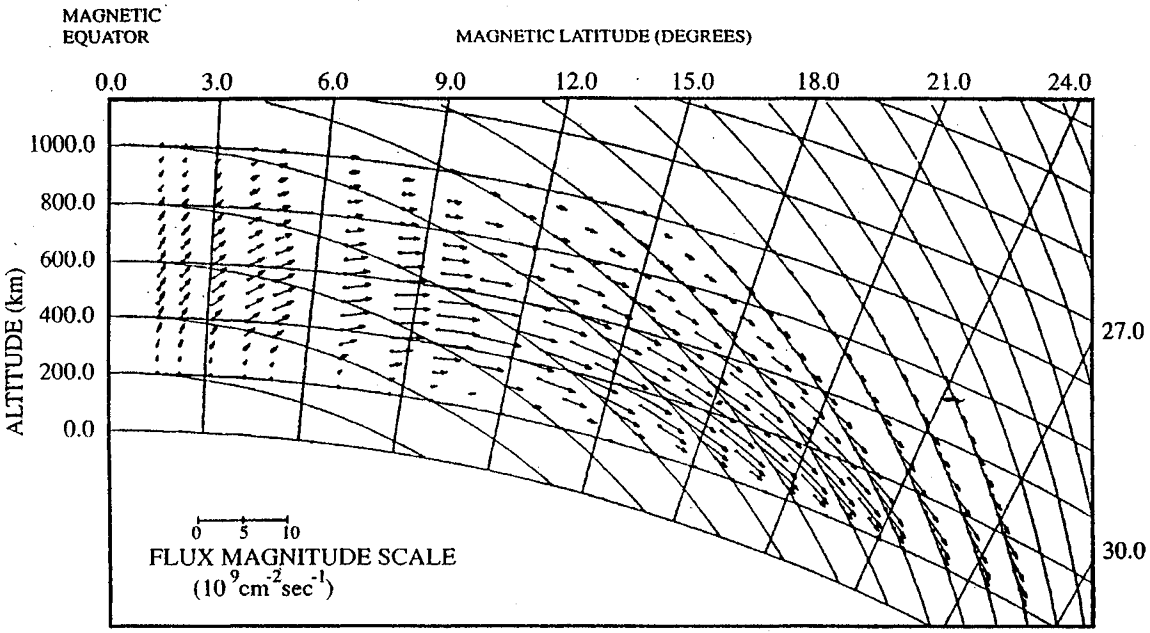

Plasma drift pattern at low latitudes due to the combined action of an upward **E** × **B** drift near the magnetic equator and a downward diffusion along **B**.[31]

Fig. 05

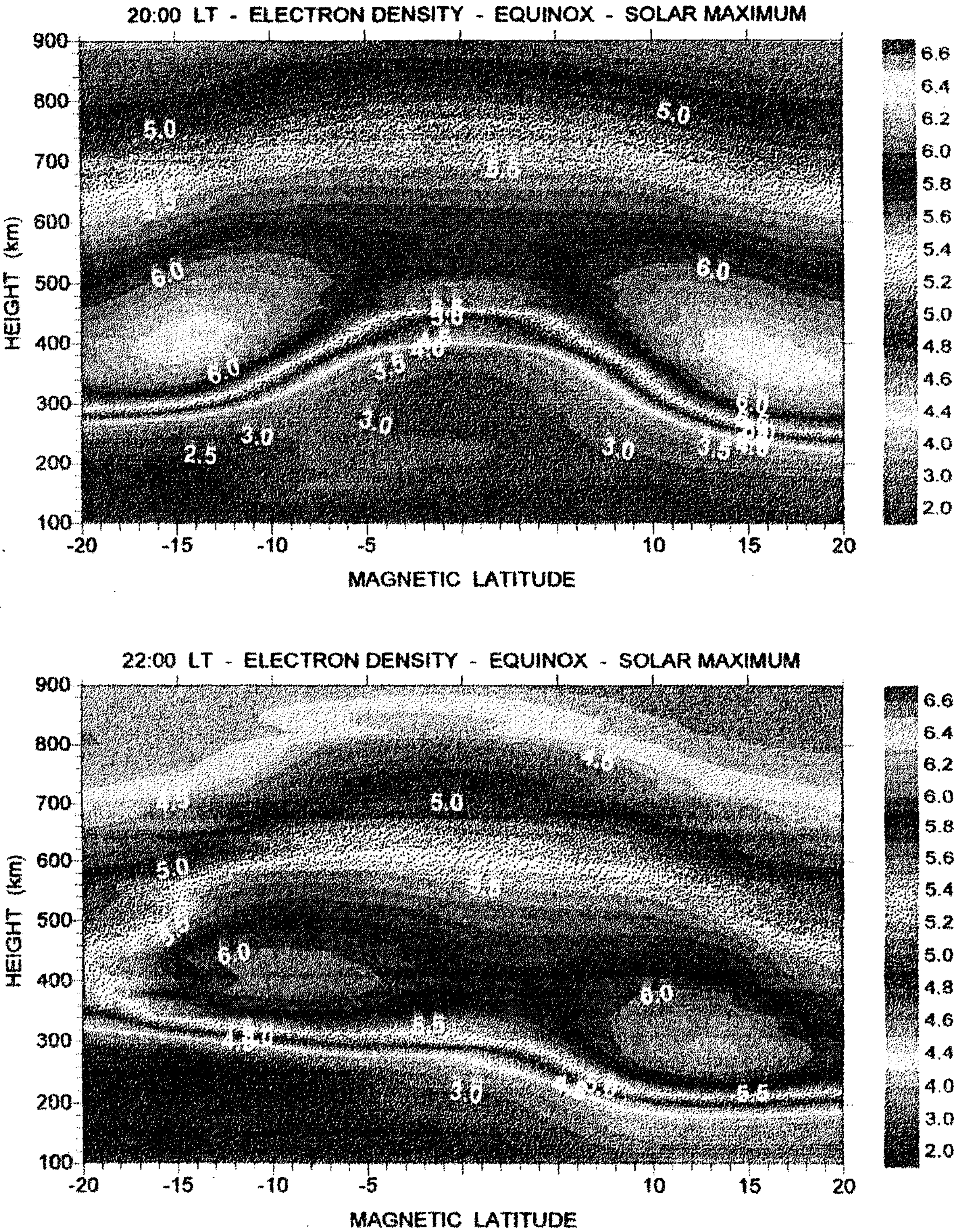

Electron density distribution (expressed as log10 in units of cm-3) as a function of height and magnetic latitude in the magnetic meridional plane for the Brazilian longitudinal sector.

Fig. 06a

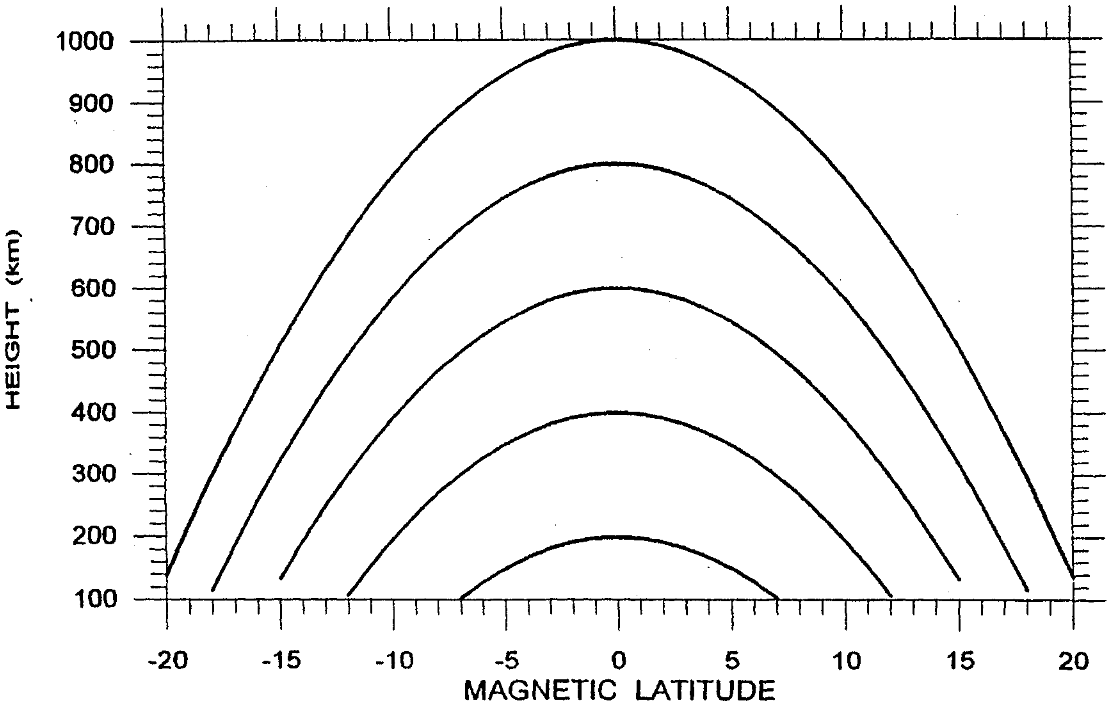

Magnetic field line geometry for the geophysical grid (height versus magnetic latitude) used in the ionospheric colour maps.

Fig. 06c

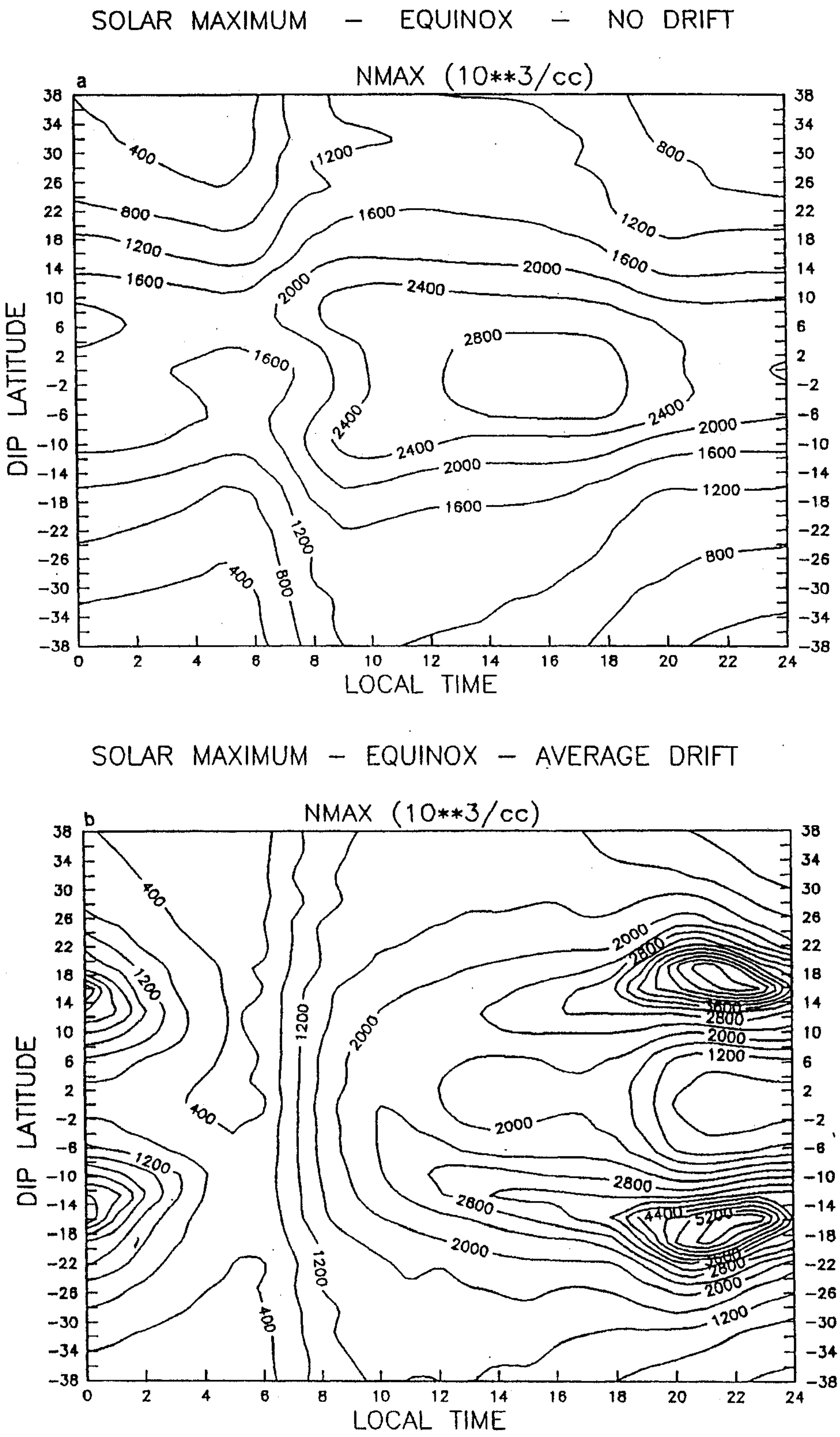

$N_{\max}$, in units of 10^3 electrons/cm^3, for equinox solar maximum for (*a*) no vertical drift, (*b*) averag vertical drift, and (*c*) high vertical drift.

Fig. 07ab

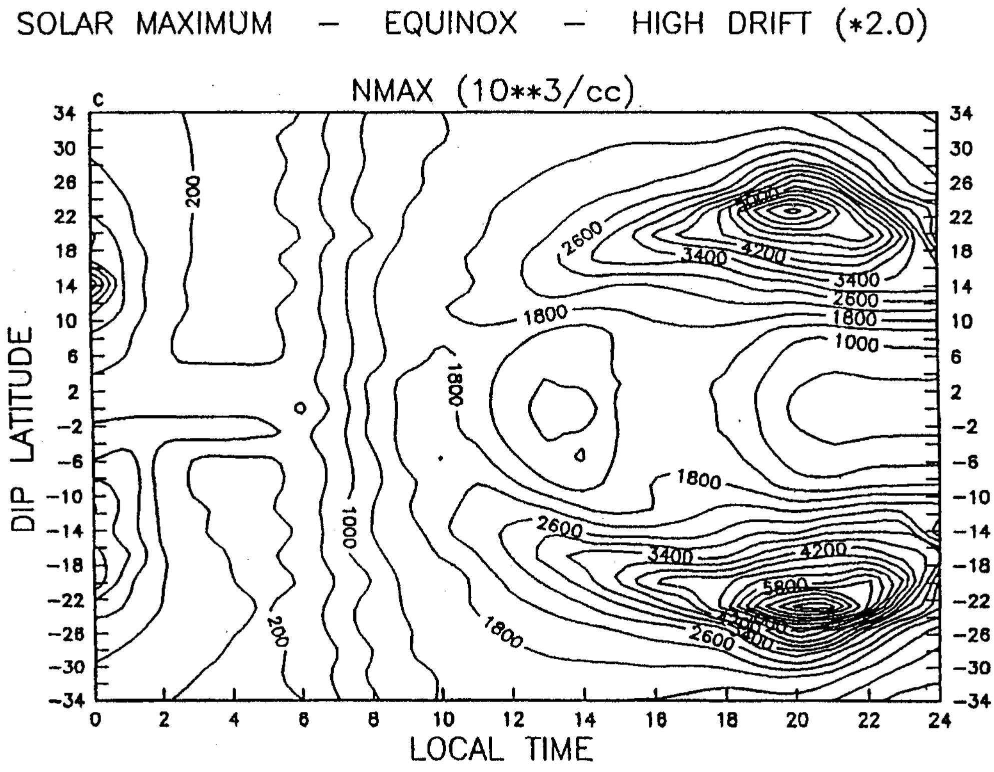
SOLAR MAXIMUM – EQUINOX – HIGH DRIFT (*2.0)
c
NMAX (10**3/cc)
DIP LATITUDE
LOCAL TIME
34
30
26
22
18
14
10
6
2
-2
-6
-10
-14
-18
-22
-26
-30
-34
0
2
4
6
8
10
12
14
16
18
20
22
24
200
1000
1800
2600
3400
4200
5800
1000
1800

Fig. 07c

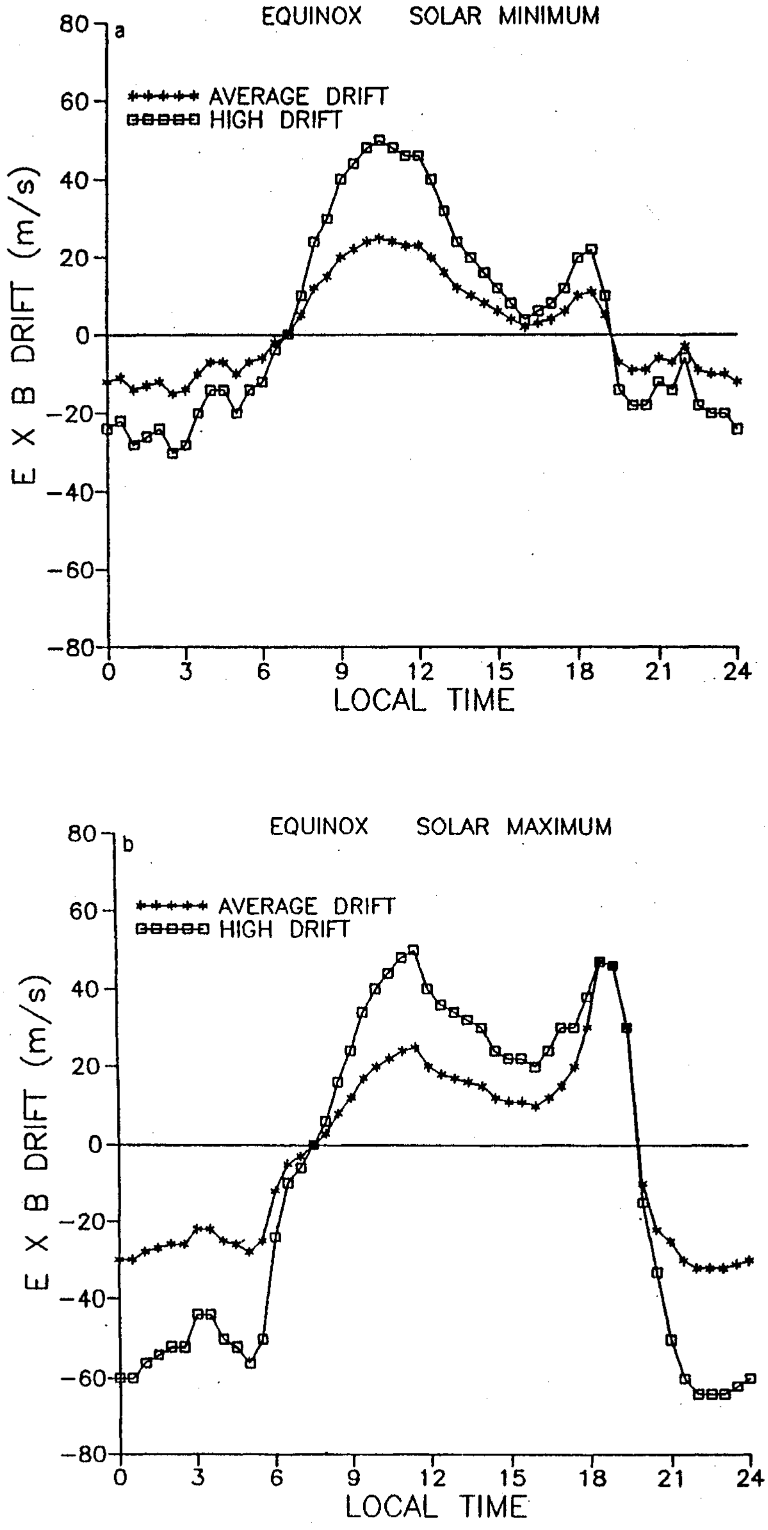

(*a*) Vertical drift for equinox, solar minimum. (*b*) Vertical drift for equinox, solar maximum.

Fig. 07d

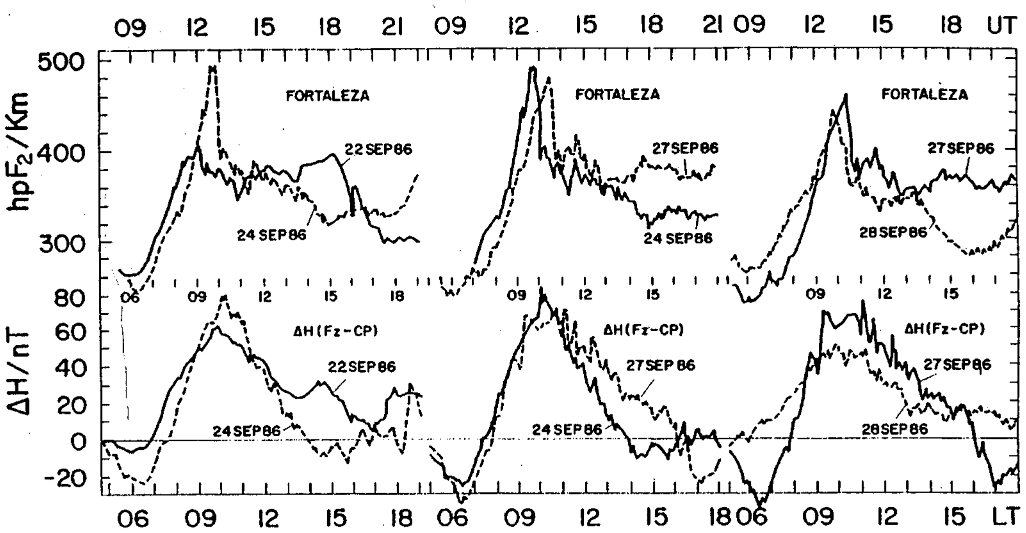

F-layer peak height (h_pF_2) variations over the magnetic equatorial station, Fortaleza and the electrojet intensity represented by ΔH(Fz-CP), namely, the difference between the ΔH variation over Fortaleza and that over Cachoeira Paulista, plotted for three pairs of days. It may be noted that morning counter electrojets were present on 24 and 27 September 86.

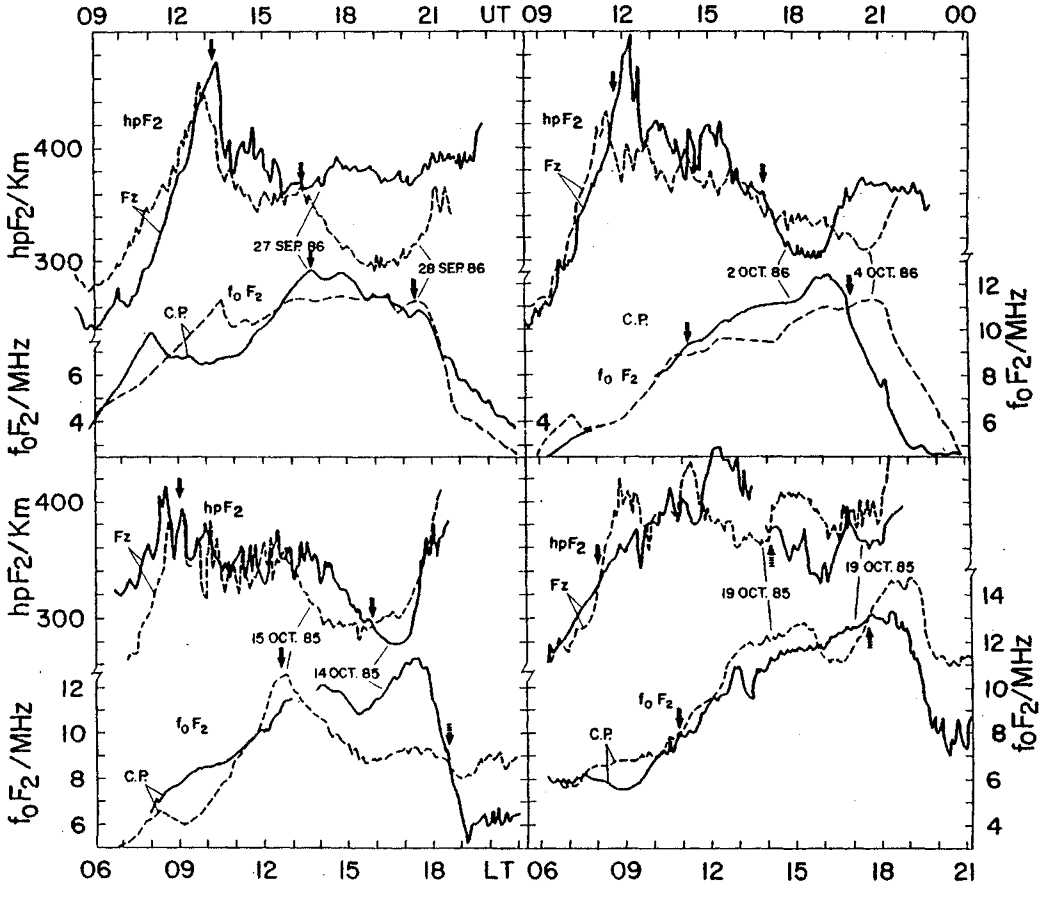

Comparison of daytime variations in h_pF_2 over Fortaleza and Cachoeira Paulista for four pairs of days, to illustrate the response of the EIA *crest ionization to changes in the F-layer peak height over the equator. The corresponding feature in the two parameters, such as cross over points or dominant peaks, are indicated by identical arrows.*

Fig. 08

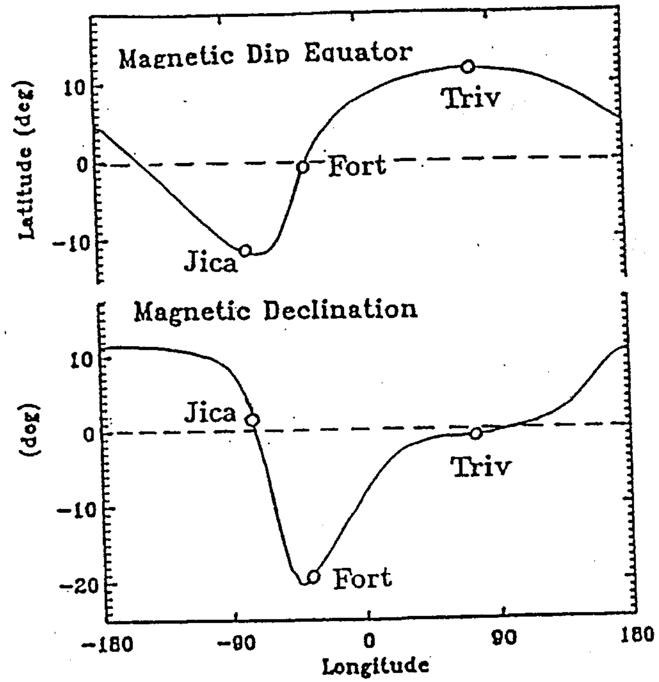

Variation of magnetic declination angle and dip equator.

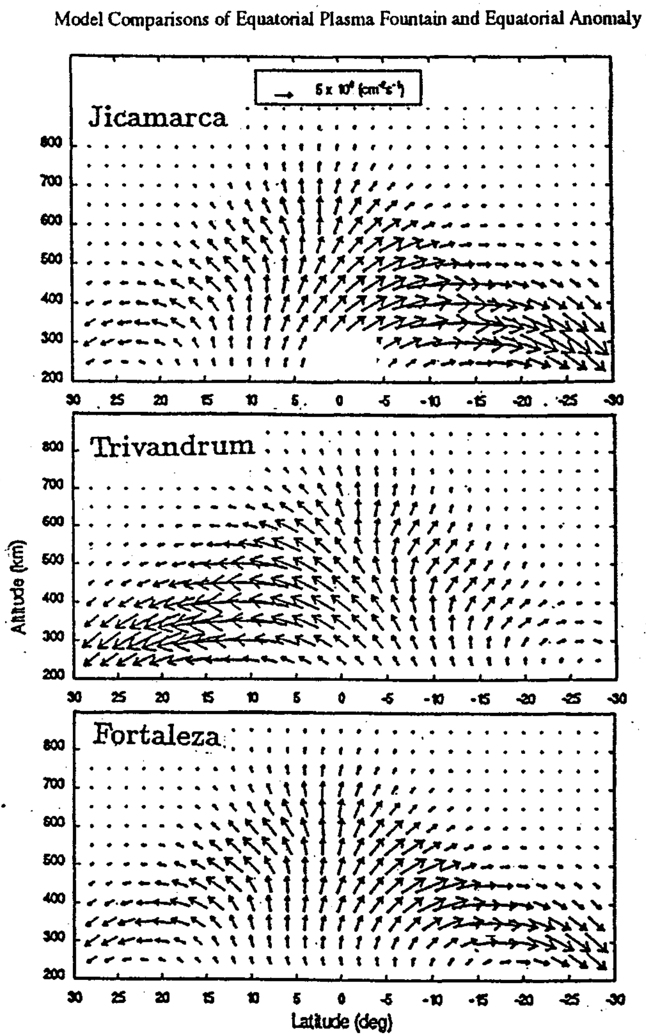

Model Plasma fountains at 12:00 LT; the flux vectors are shown in linear scale; the minimum vector length (zero length) corresponds to plasma fluxes less than 5×10^6 cm^{-2} s^{-1}; positive latitude is northwards.

Fig. 09

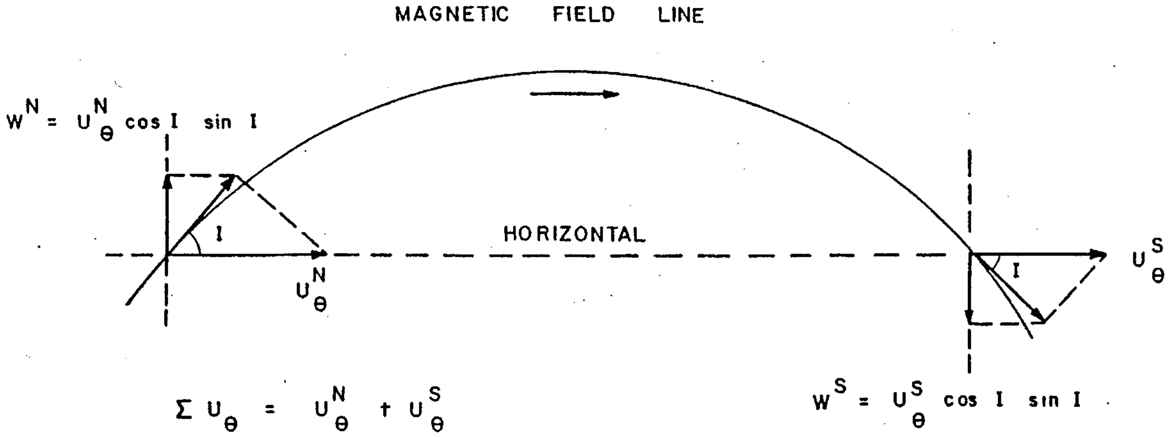

Schematic diagram illustrating the vertical plasma drift (w) produced by the horizontal thermospheric wind component along the magnetic meridian (u_θ). The magnetic dip angle is denoted by I.

Fig. 09a

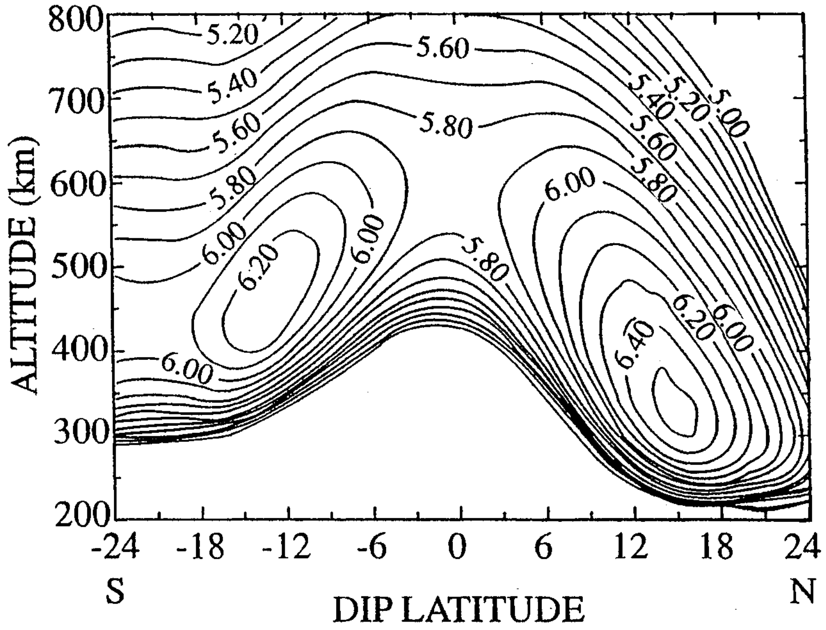

Calculated electron density contours ($\log_{10} n_e$) as a function of altitude and dip latitude at 2000 LT for December solstice conditions.[32]

Fig. 10

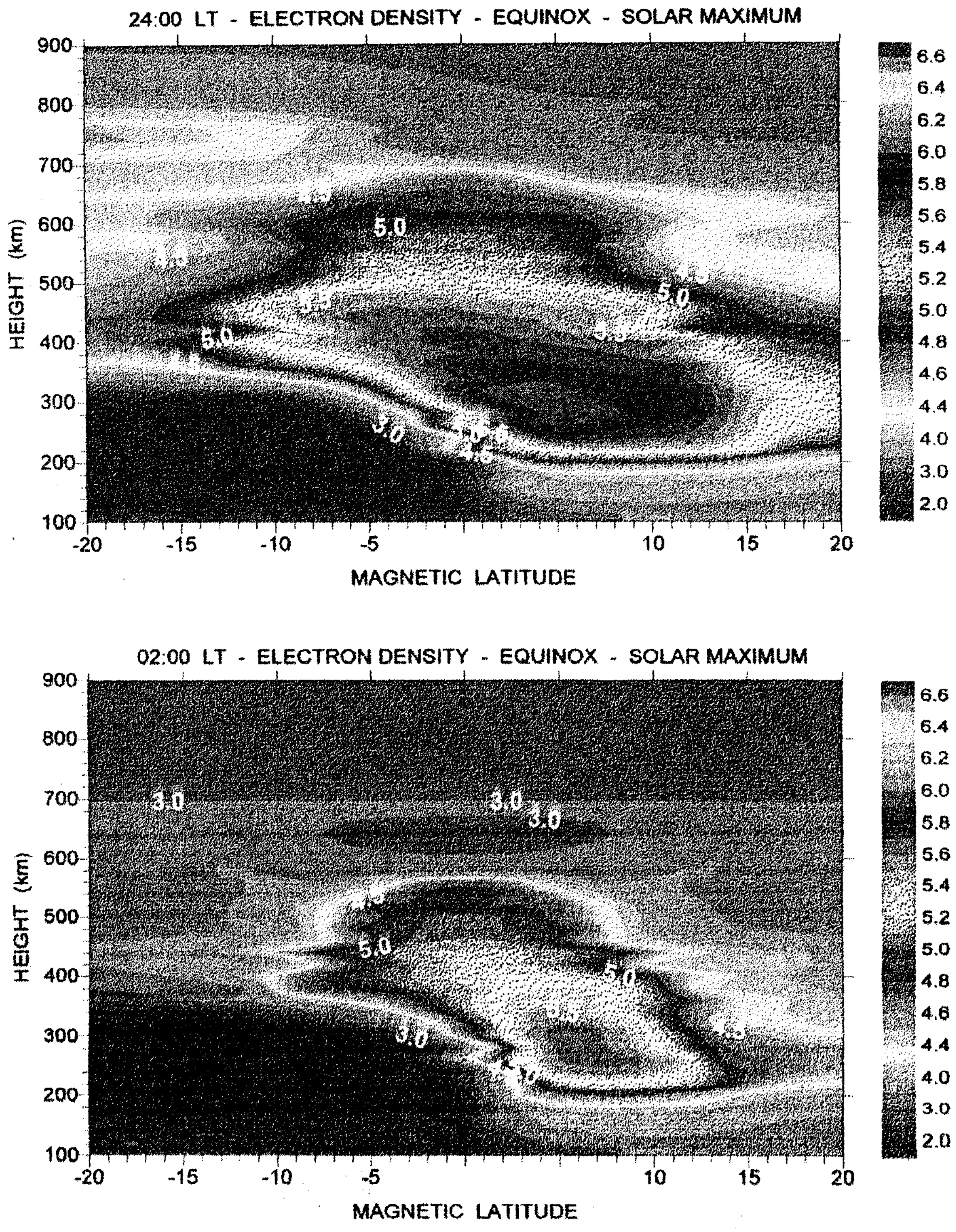

Electron density distribution (expressed as log10 in units of cm-3) as a function of height and magnetic latitude in the magnetic meridional plane for the Brazilian longitudinal sector.

Fig. 10b

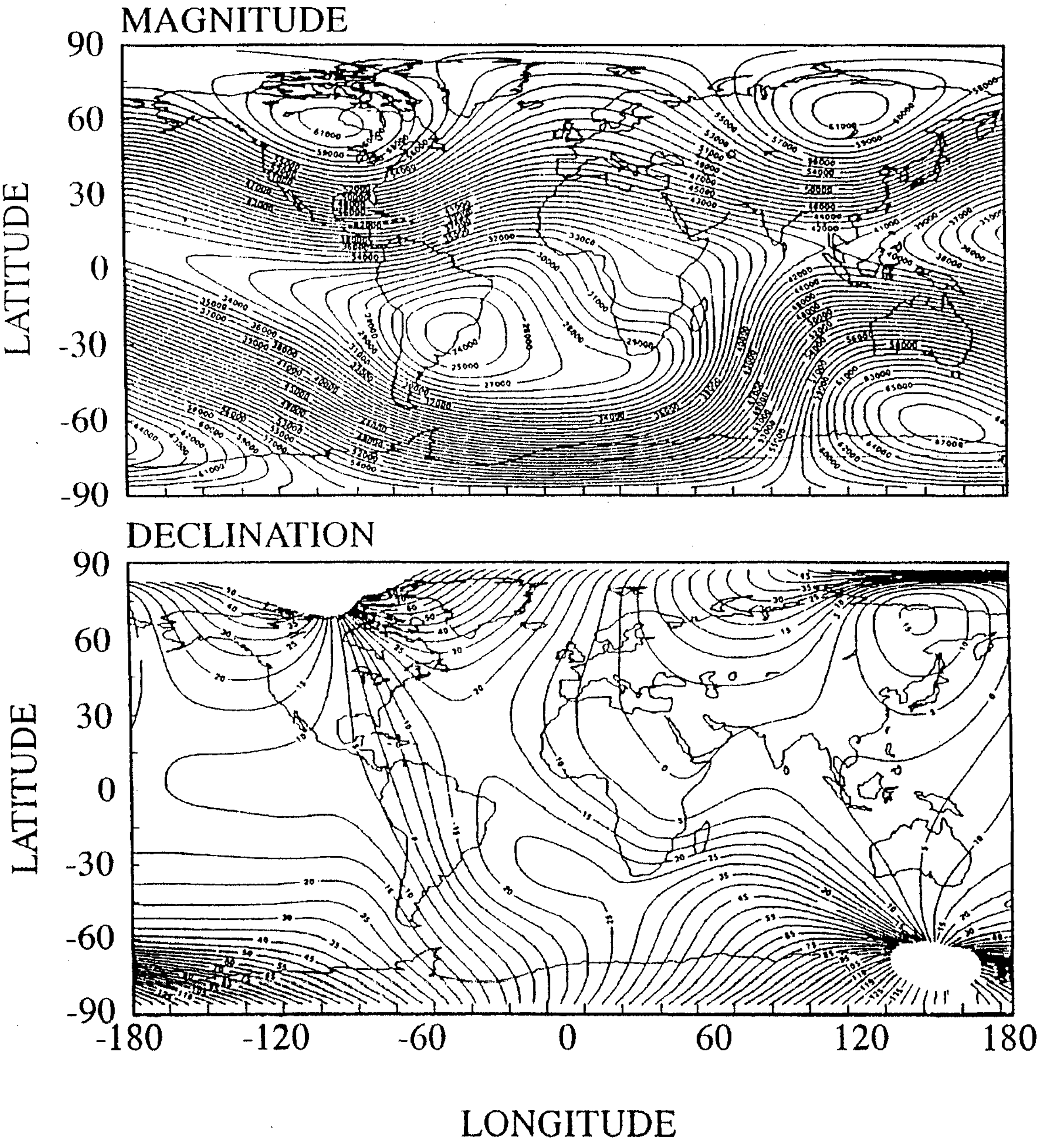

Magnitude of the geomagnetic field (top) and declination angle in degrees (bottom) at the Earth's surface.[6]

Fig. 11

Fig.12 a

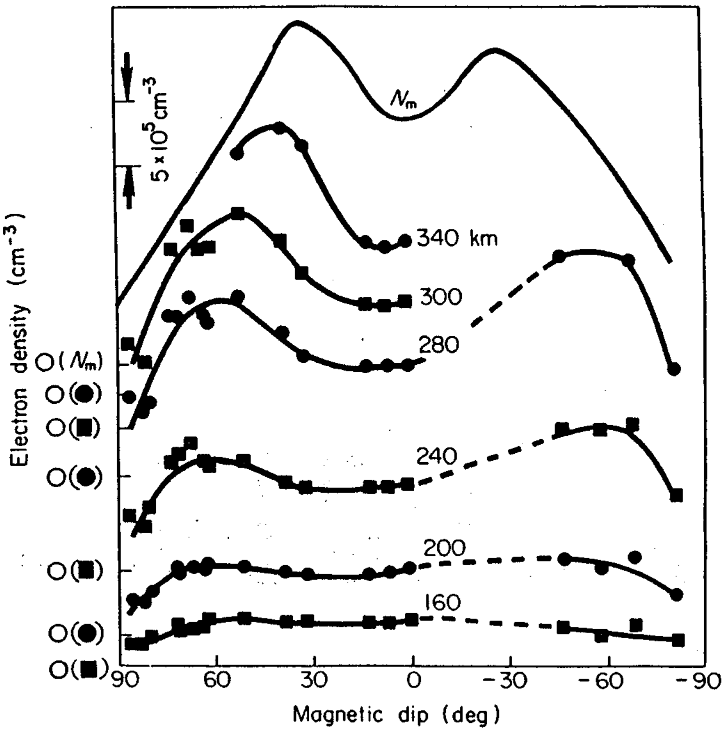

Variation of N_mF2 and of electron density (electron concentration) at fixed heights with magnetic dip, for noon on magnetically quiet days in September 1957. The zero level for each curve is indicated on the left [after Croom *et al.* (1959)].

Fig.12 b

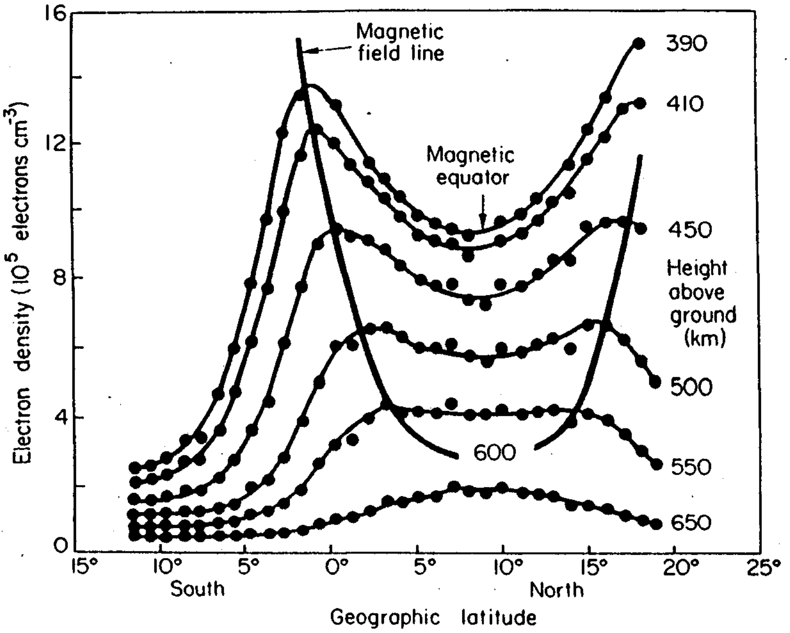

Latitude variation of electron density (electron concentration) at fixed heights, determined by means of the Alouette I topside sounder satellite above Singapore (1°N, 104°E) at 1234 local time, 15 September 1963. A magnetic field line is shown [King *et al.* (1967d)].

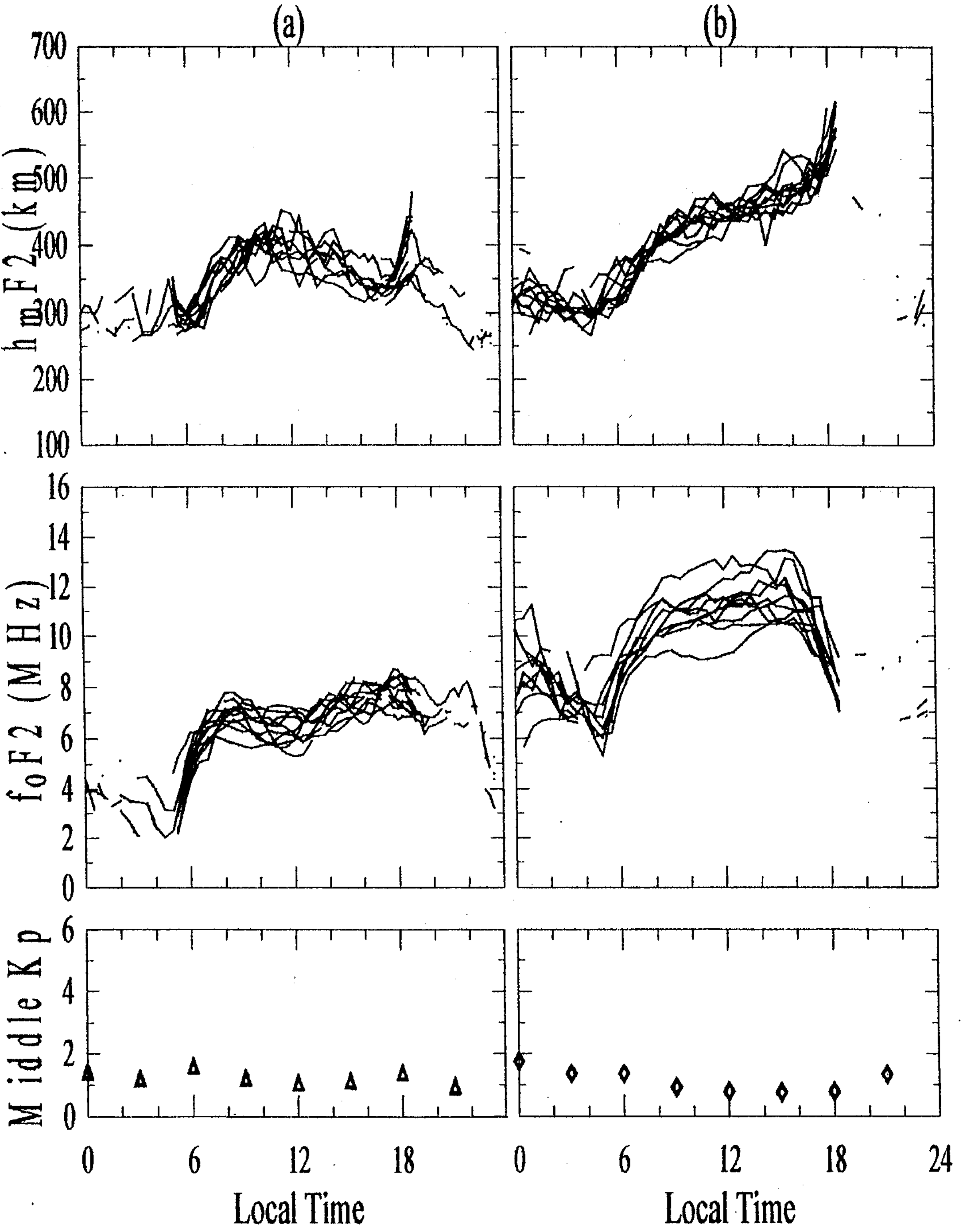
(a)
(b)
700
600
500
400
300
200
100
h m F 2 (k m)
16
14
12
10
8
6
4
2
0
f o F 2 (M H z)
6
4
2
0
M i d d l e K p
0
6
12
18
24
Local Time
Local Time

Fig. 13a

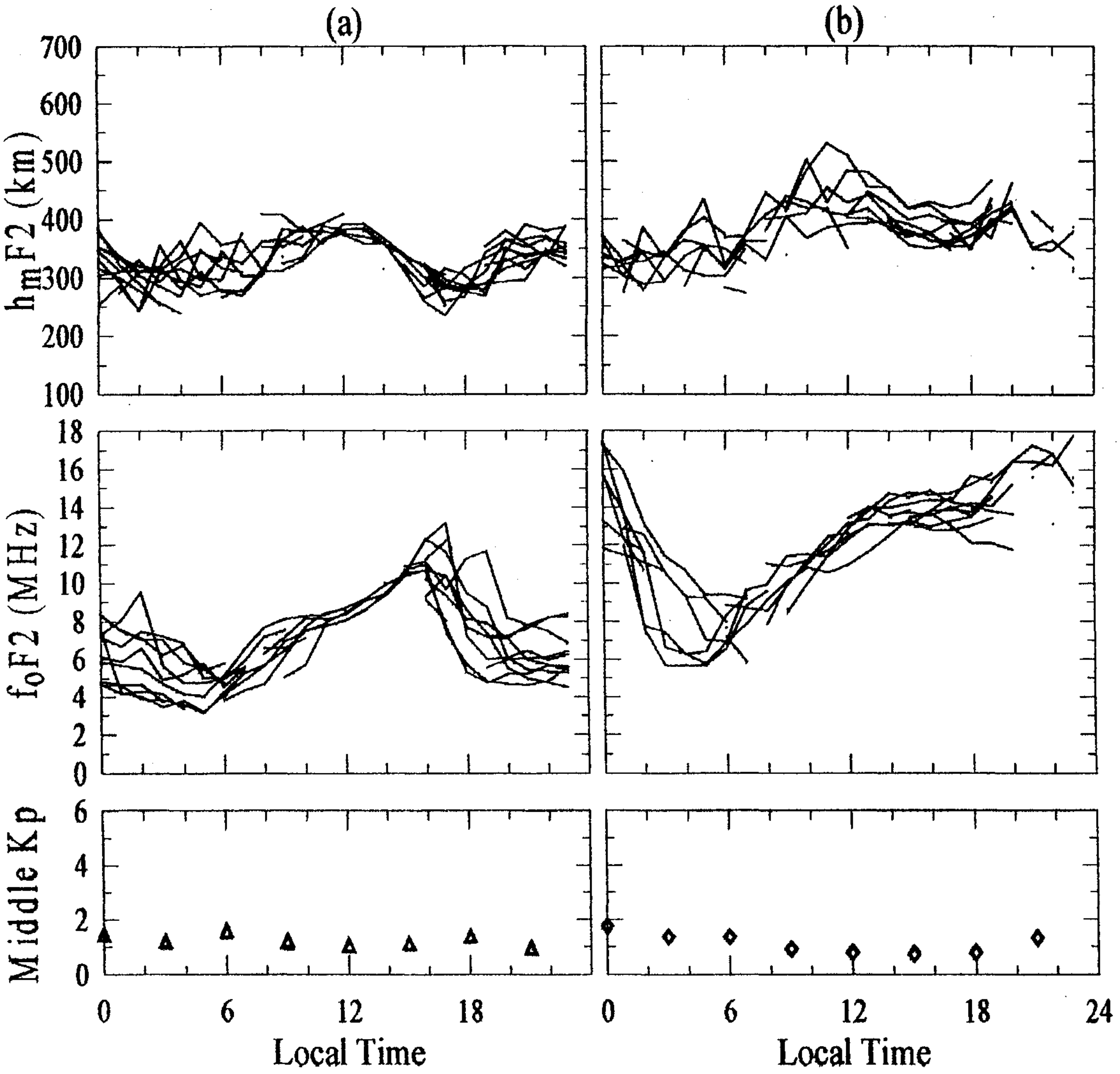
(a)
(b)
hmF2 (km)
700
600
500
400
300
200
100
foF2 (MHz)
18
16
14
12
10
8
6
4
2
0
Middle Kp
6
4
2
0
0
6
12
18
24
Local Time
Local Time

Fig. 13b

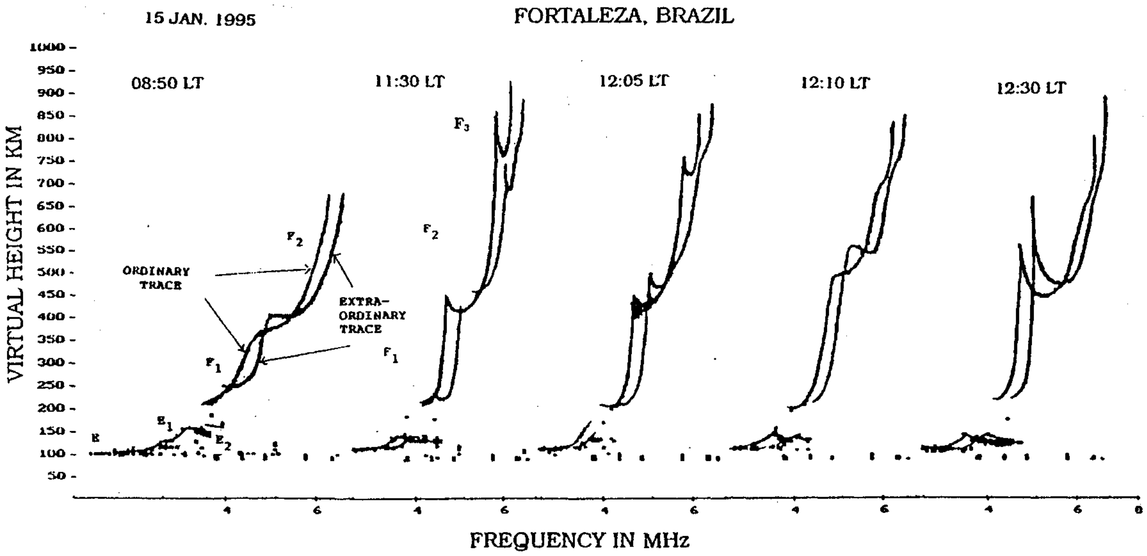

Sample ionograms recorded at Fortaleza on January 15, 1995. Note the development and decay of the F_3 layer as an additional trace at the high-frequency end at the virtual altitude of about 750 km, which is most distinct at 1130 LT.

Fig. 14

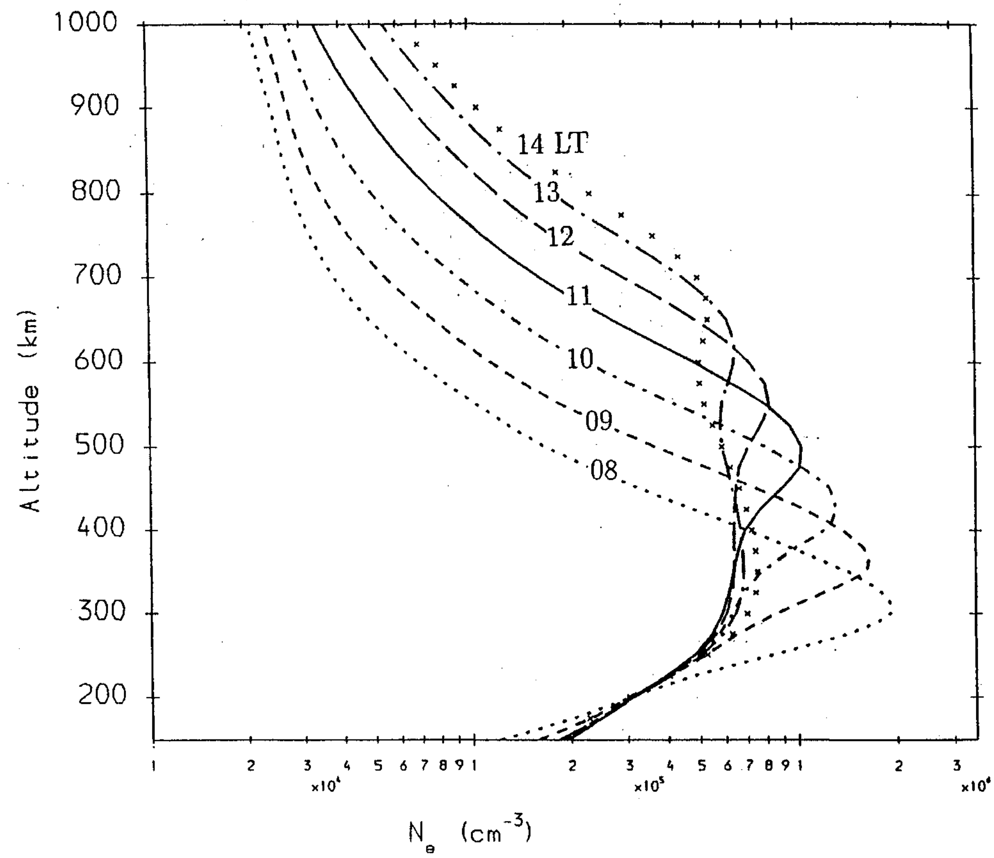

Model electron density profiles for the longitude of Fortaleza under conditions of strongest F_3 layer.

Fig. 15

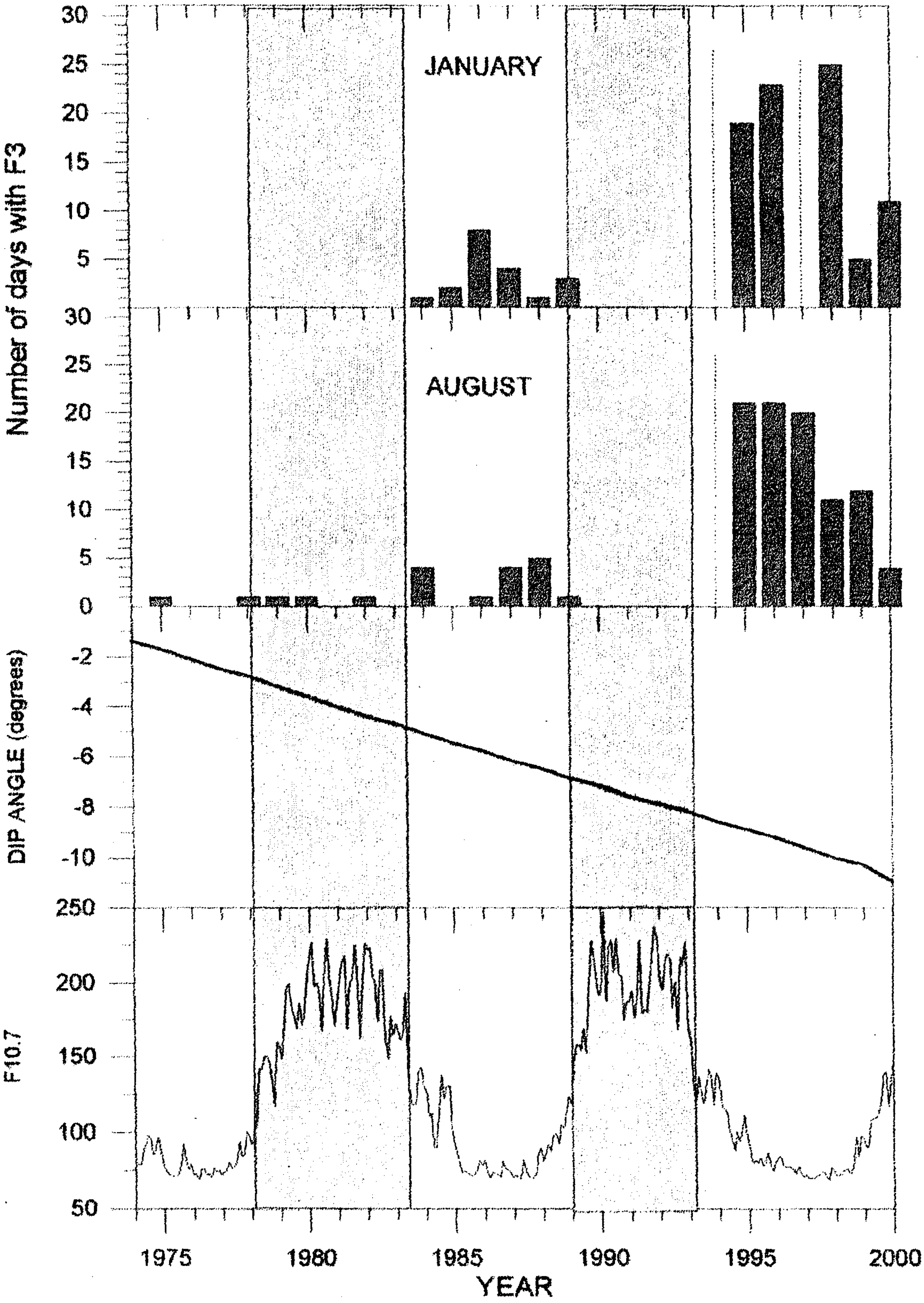
Number of days with F3
JANUARY
AUGUST
30
25
20
15
10
5
0
DIP ANGLE (degrees)
-2
-4
-6
-8
-10
F10.7
250
200
150
100
50
1975
1980
1985
1990
1995
2000
YEAR

Fig. 16

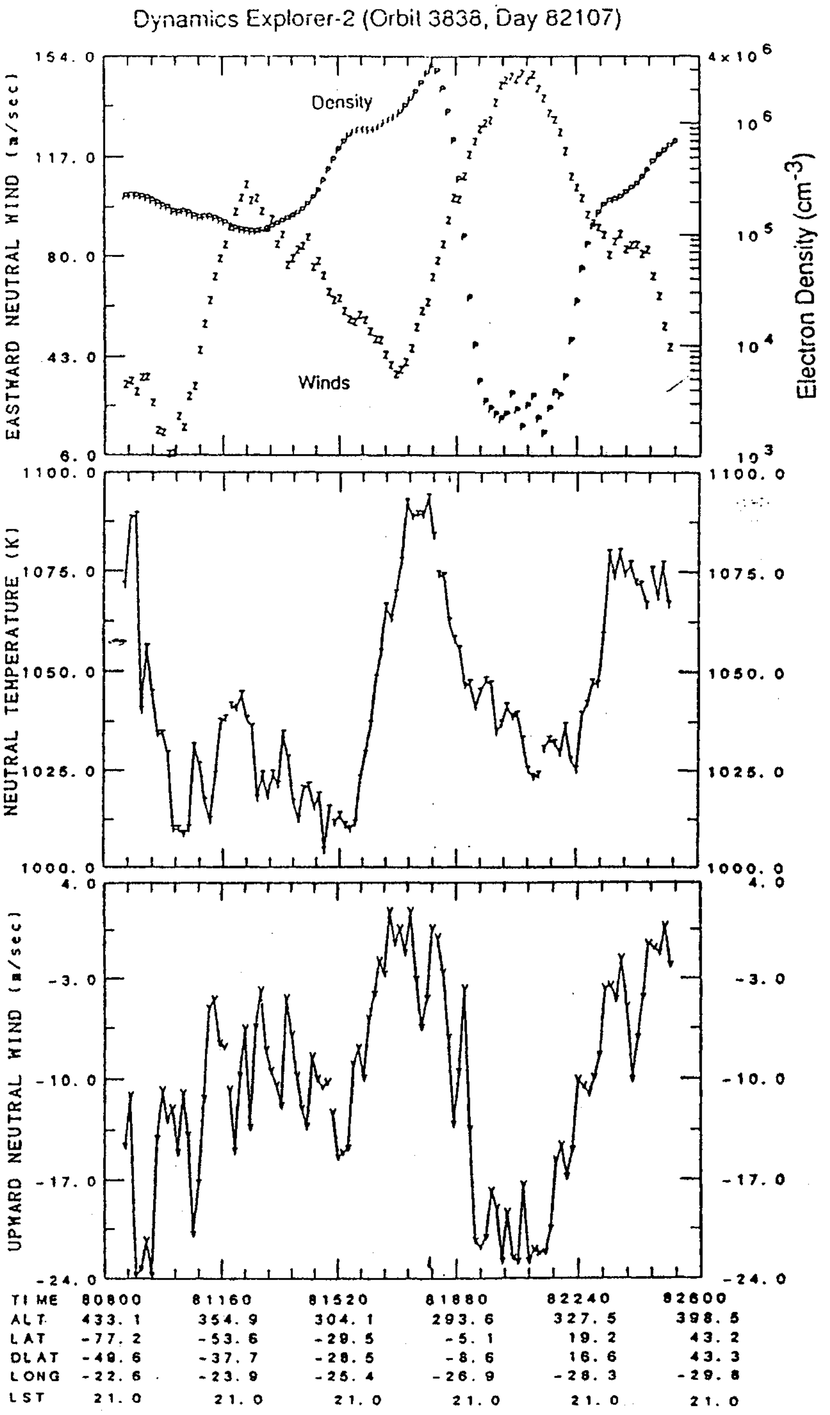

DE-2 data of electron density zonal winds (upper panel) neutral temperature (middle panel) and vertical winds (lower panel) on April 17, 1982 at 2100 hrs LST and around the longitude 27W.

Fig. 17

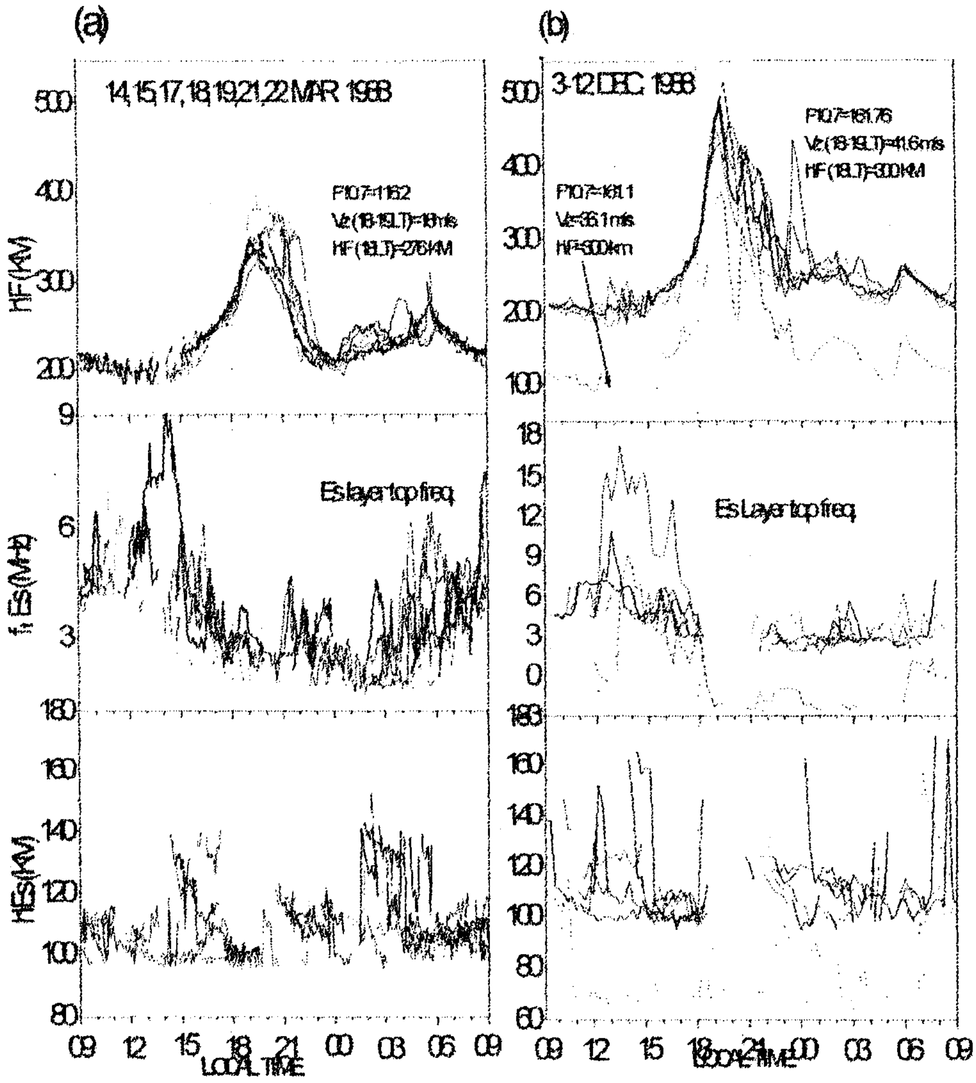
(a)
14,15,17,18,19,21,22 MAR 1988
F10.7=116.2
Vz(18-19LT)=18m/s
HF(18LT)=276KM
hF(KM)
500
400
300
200
9
6
3
Es layer top freq
f_t Es(MHz)
180
160
140
120
100
80
hEs(KM)
09
12
15
18
21
00
03
06
09
LOCAL TIME
(b)
3-12 DEC 1988
F10.7=161.1
Vz=36.1m/s
HF=300km
F10.7=161.76
Vz(18-19LT)=41.6m/s
HF(18LT)=300KM
500
400
300
200
100
18
15
12
9
6
3
0
Es Layer top freq
180
160
140
120
100
80
60
09
12
15
18
21
00
03
06
09
LOCAL TIME

Fig. 18

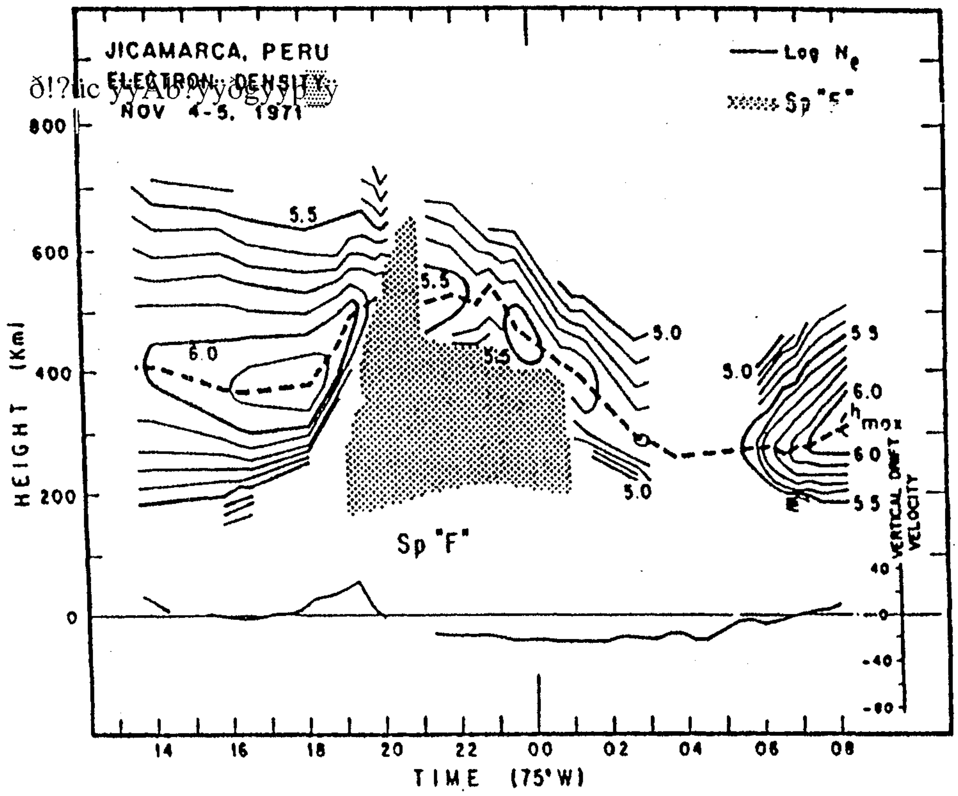

Figure 1. Typical *F* region electron density profile vertical plasma drift profiles measured by the 50 Mhz Jicamarca incoherent scatter radar. The dotted area indicates the occurrence of spread *F* echoes.

Fig. 18a

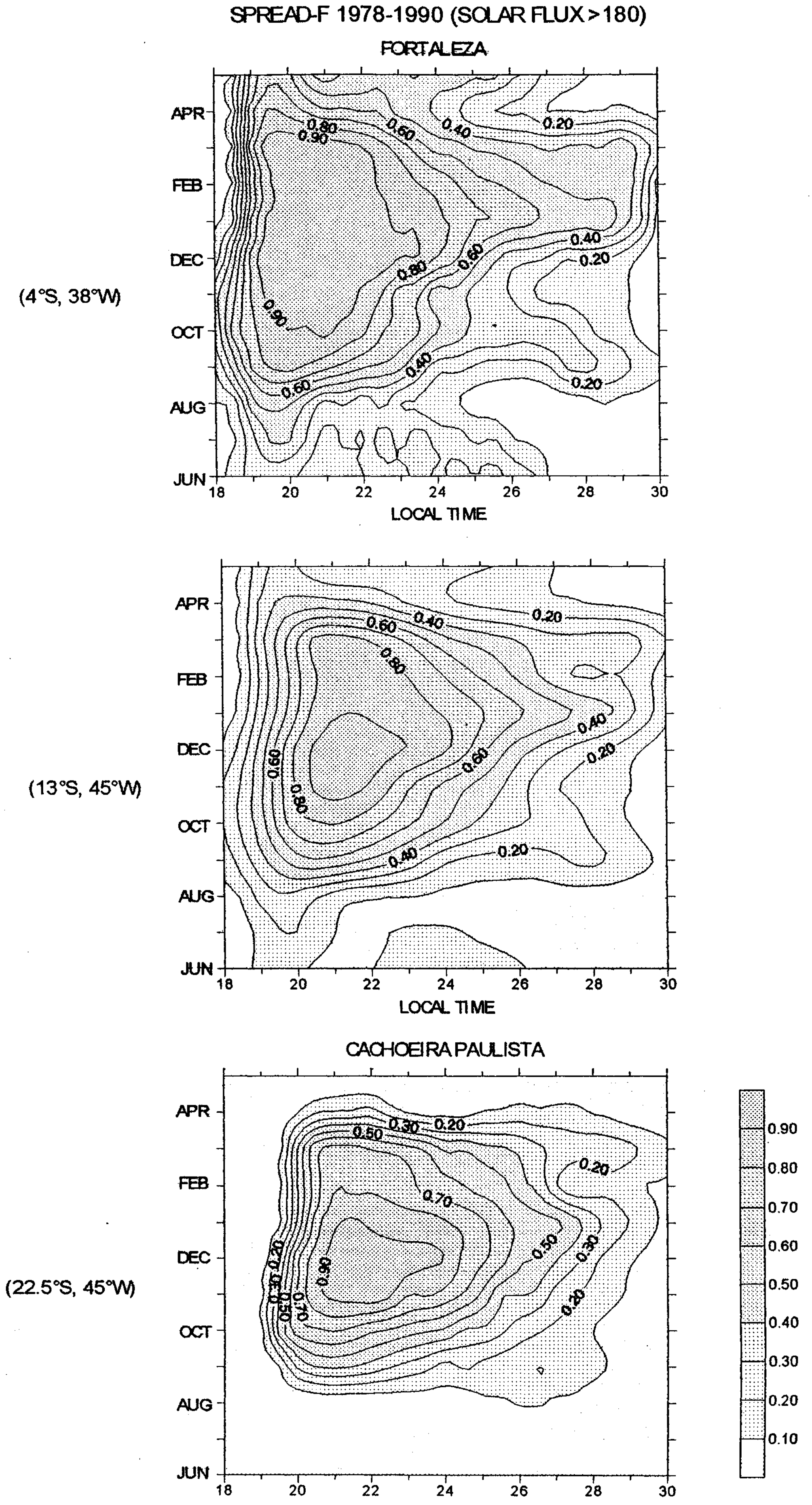
SPREAD-F 1978-1990 (SOLAR FLUX>180)
FORTALEZA
(4°S, 38°W)
(13°S, 45°W)
CACHOEIRA PAULISTA
(22.5°S, 45°W)
APR
FEB
DEC
OCT
AUG
JUN
18
20
22
24
26
28
30
LOCAL TIME
0.90
0.80
0.70
0.60
0.50
0.40
0.30
0.20
0.10

Fig. 19

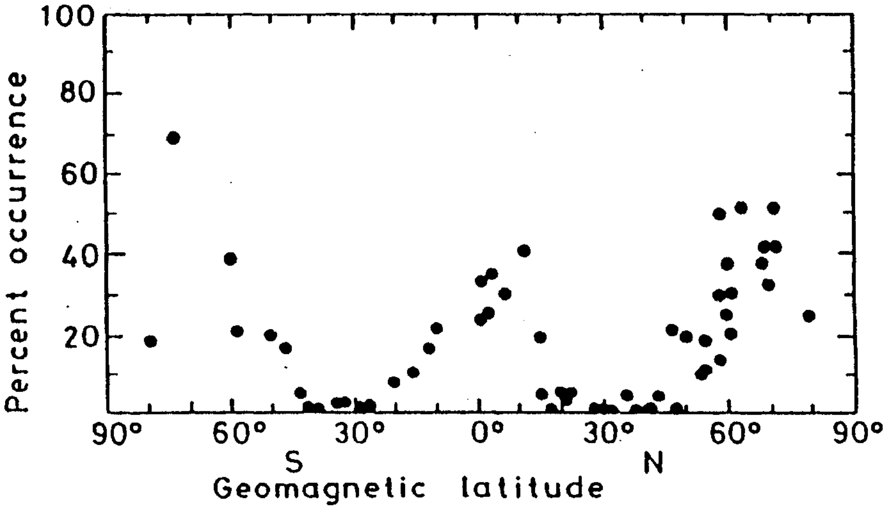

Occurrence of spread-F as a function of geomagnetic latitude during August–September 1957. (T. Shimazaki, *J. Radio Res. Lab. Japan* 6, 669, 1959)

Fig. 20a

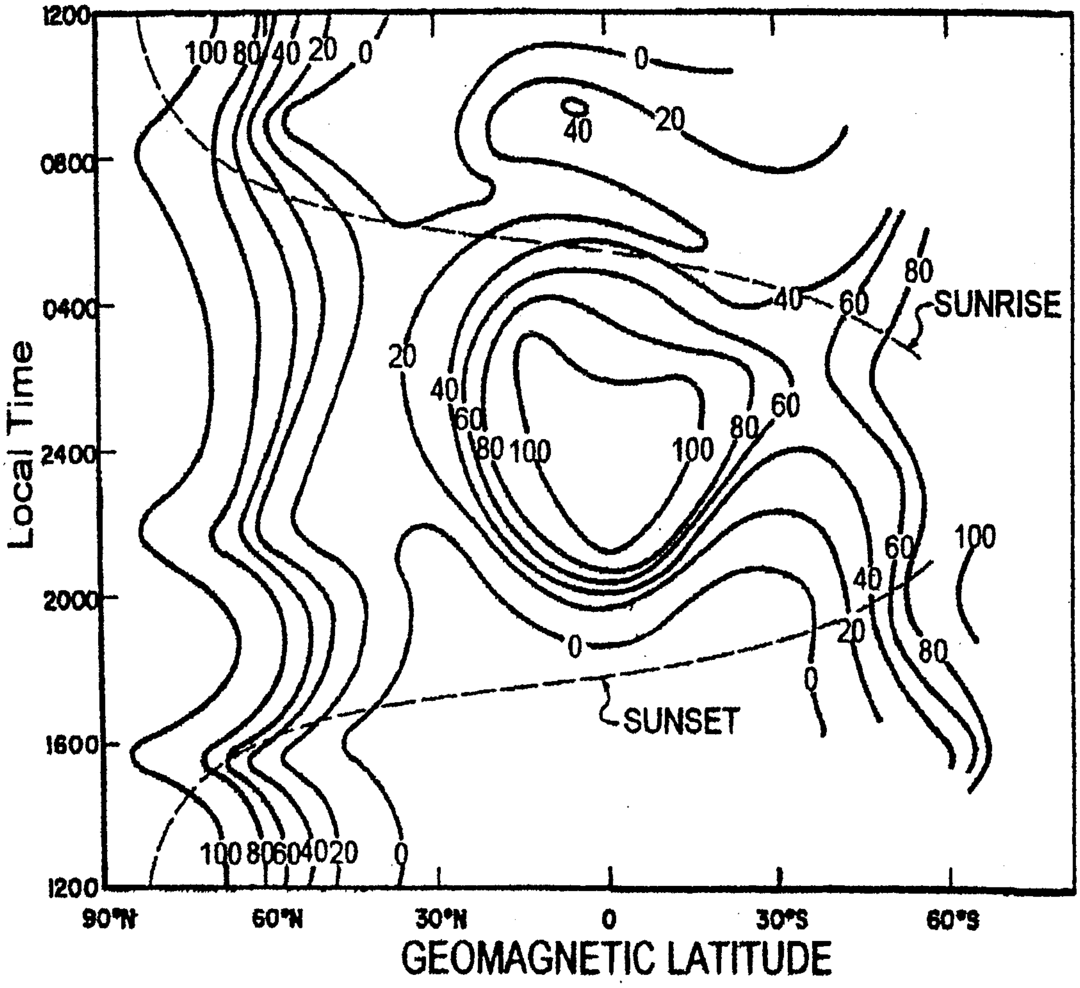
1200
0800
0400
2400
2000
1600
1200
Local Time
90°N
60°N
30°N
0
30°S
60°S
GEOMAGNETIC LATITUDE
100
80
40
20
0
0
40
20
20
40
60
80
100
100
80
60
40
60
80
SUNRISE
60
100
40
20
80
0
0
SUNSET
100
80
60
40
20
0

Fig. 20b

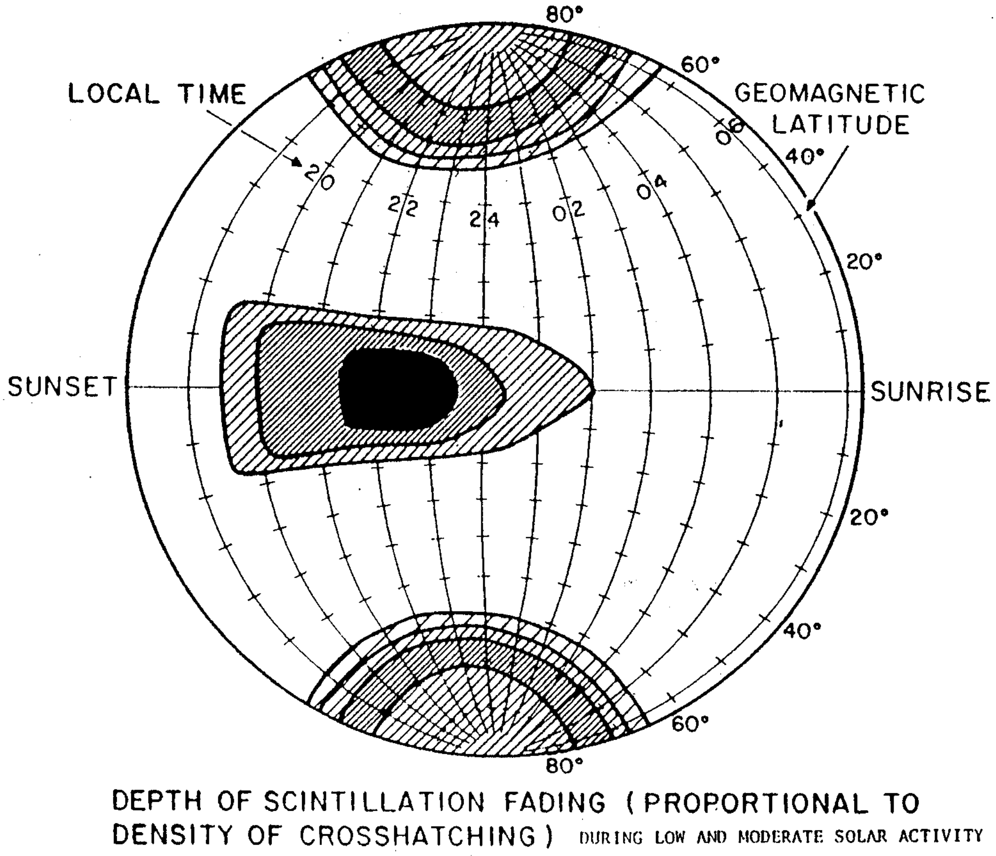

Global depth of scintillation fading (proportional to density of crosshatching) during low and moderate solar activity.

Fig. 21

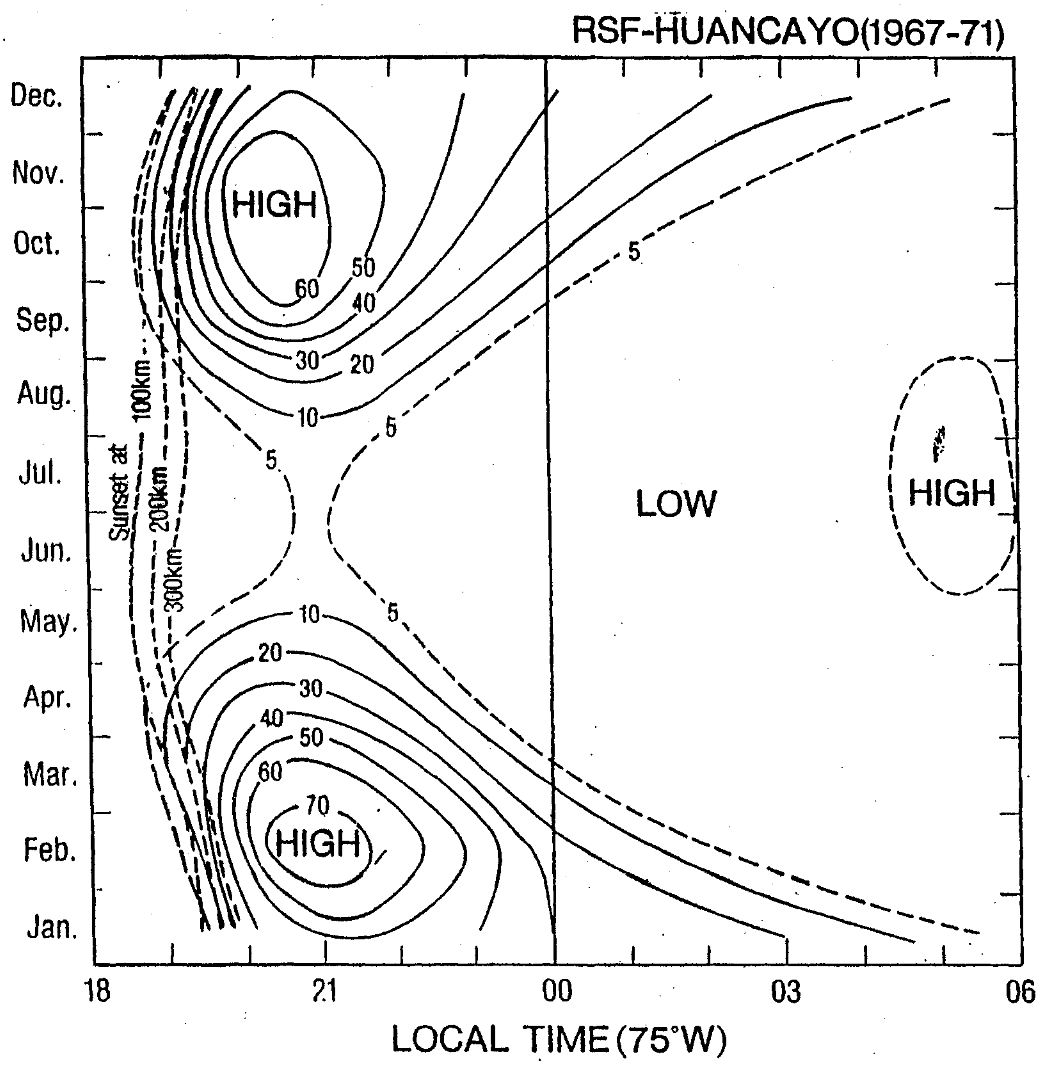
RSF-HUANCAYO(1967-71)
Dec.
Nov.
Oct.
Sep.
Aug.
Jul.
Jun.
May.
Apr.
Mar.
Feb.
Jan.
HIGH
60
50
40
30
20
10
5
5
10
5
20
30
40
50
60
70
HIGH
LOW
HIGH
Sunset at
100km
200km
300km
18
21
00
03
06
LOCAL TIME (75°W)

Fig. 22

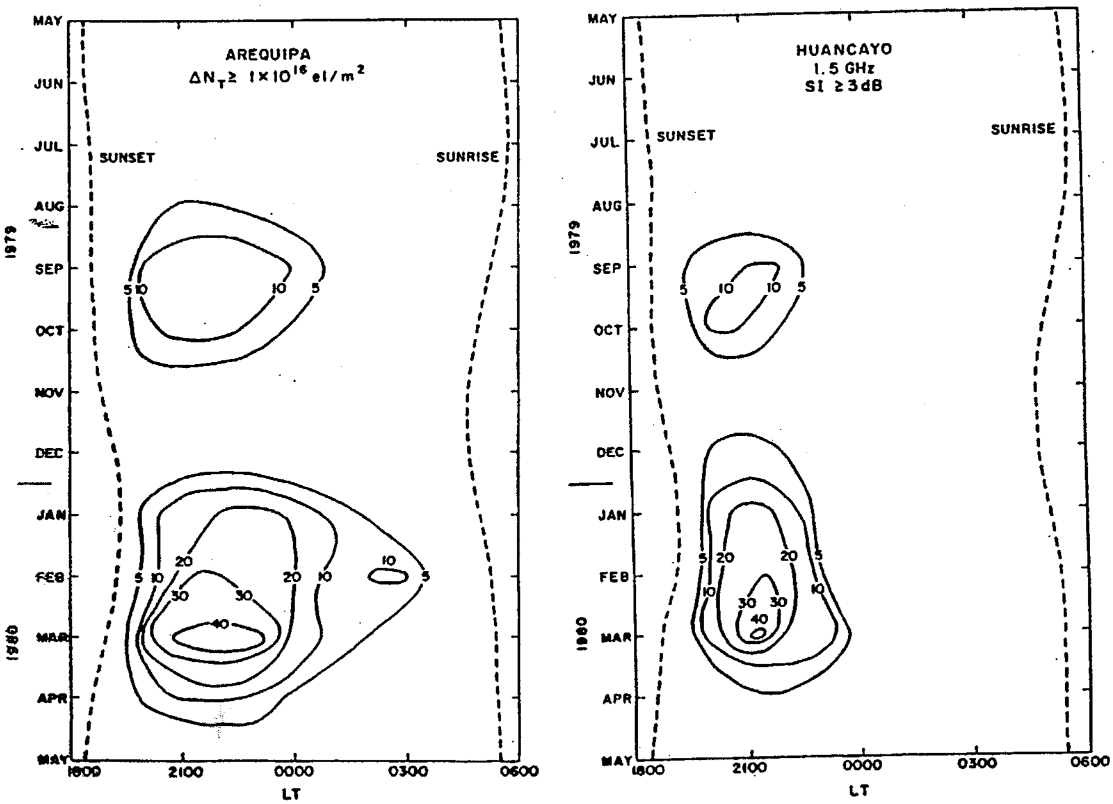

Monthly percentage occurrence contours of ionospheric electron content depletions ≥ 1 x 10^{16} el/m^2 at Arequipa during May 1979 – May 1980.

Monthly percentage occurrence contours of scintillations at 1.54 GHz (SI ≥ 3 dB) observed at Huancayo.

Fig. 23

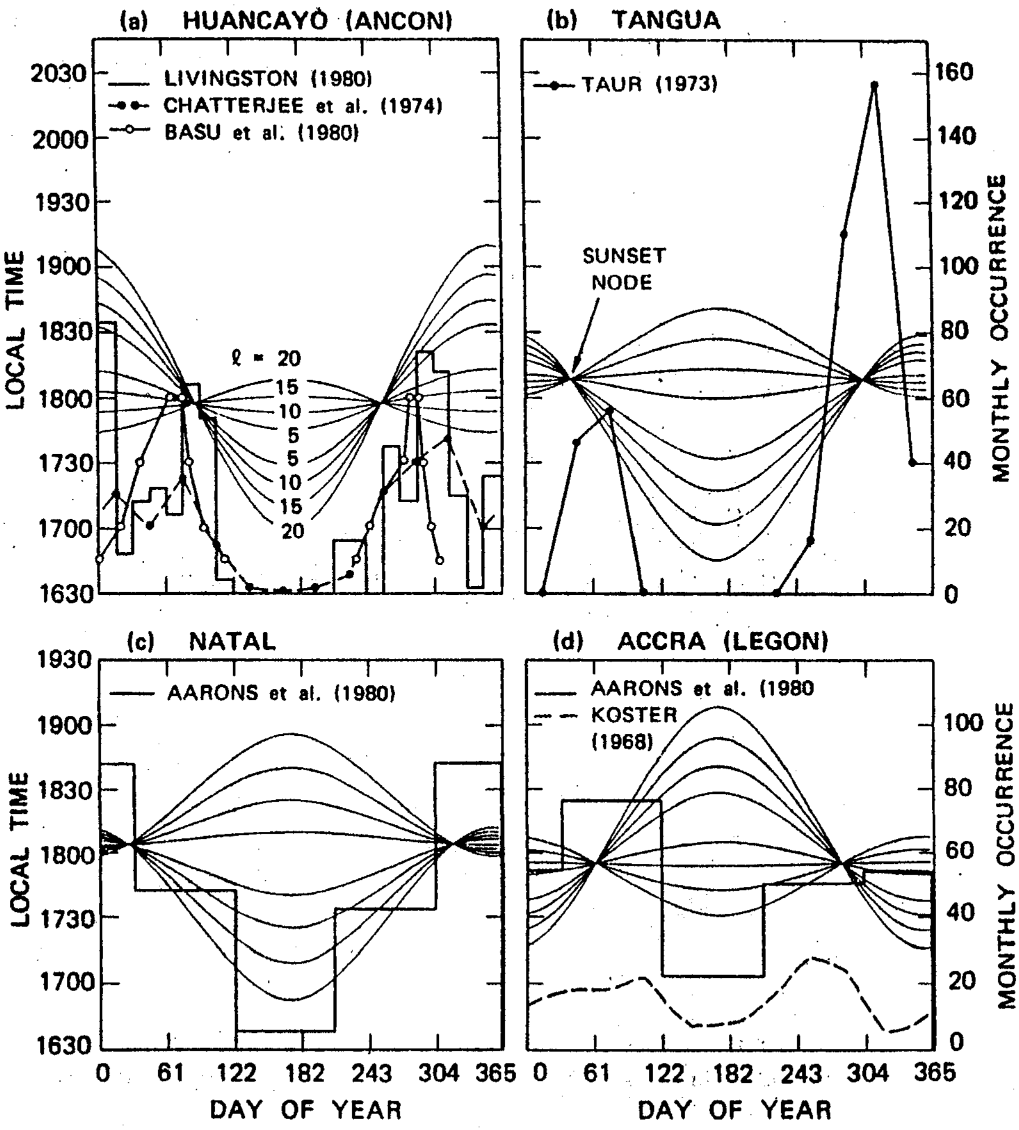

Fig. 3. Comparison of the times of equatorial scintillation maximum to those of the sunset nodes, American-African sector.

Fig. 24